Biological Applications of Short Wavelength Microscopy Based on Compact, Laser-Produced Gas-Puff Plasma Source

Alfio Torrisi [1,†] , **Przemysław W. Wachulak** [2,*,†], **Andrzej Bartnik** [2], **Łukasz Węgrzyński** [2], **Tomasz Fok** [2] **and Henryk Fiedorowicz** [2]

1   Nuclear Physics Institute, Czech Academy of Sciences, 25068 Řež, Czech Republic; torrisi@ujf.cas.cz
2   Institute of Optoelectronics, Military University of Technology, 00-908 Warsaw, Poland;
    andrzej.bartnik@wat.edu.pl (A.B.); lukasz.wegrzynski@wat.edu.pl (L.W.); tomasz.fok@wat.edu.pl (T.F.);
    henryk.fiedorowicz@wat.edu.pl (H.F.)
*   Correspondence: przemyslaw.wachulak@wat.edu.pl
†   A.T. and P.W. contribution to this work was equal.

Featured Application: **Short wavelength compact microscopy setups, operating in the biological-dedicated "water window" spectral range, perform sample imaging with a nanometer spatial resolution, employing complementary tools to the existing imaging techniques.**

Abstract: Over the last decades, remarkable efforts have been made to improve the resolution in photon-based microscopes. The employment of compact sources based on table-top laser-produced soft X-ray (SXR) in the "water window" spectral range (λ = 2.3–4.4 nm) and extreme ultraviolet (EUV) plasma allowed to overcome the limitations imposed by large facilities, such as synchrotrons and X-ray free electron lasers (XFEL), because of their high complexity, costs, and limited user access. A laser-plasma double stream gas-puff target source represents a powerful tool for microscopy operating in transmission mode, significantly improving the spatial resolution into the nanometric scale, comparing to the traditional visible light (optical) microscopes. Such an approach allows generating the plasma efficiently, without debris, providing a high flux of EUV and SXR photons. In this review, we present the development and optimization of desktop imaging systems: a EUV and an SXR full field microscope, allowing to achieve a sub-50 nm spatial resolution with short exposure time and an SXR contact microscope, capable to resolve internal structures in a thin layer of sensitive photoresist. Details about the source, as well as imaging results for biological applications, will be presented and discussed.

1. Introduction

According to the Rayleigh criterion [1], the spatial resolution in photon-based imaging systems can be improved by decreasing the illumination wavelength. After the discovery of the X-rays by Röntgen, the major limitation for the employment of such electromagnetic radiation for microscopy was the availability of suitable sources and optics, until the 1970s. The initial promising results with high spatial resolution imaging were obtained from the X-ray microscopy setups, located at large synchrotron facilities [2], which, even if efficient, limited their access to the scientific community. Nowadays, several laboratory-based soft X-ray (SXR) sources for microscopy applications are a worldwide spread. The shorter wavelength ranges can be exploited for the observation of even smaller objects with high spatial resolution. Significant progress related to the laboratory based short

wavelength sources for microscopy has already been made, especially employing extreme ultraviolet (EUV, λ = 10–120 nm) and soft X-ray (λ = 0.1–10 nm) wavelengths [1], in the so-called "water window" spectral range (λ = 2.3–4.4 nm) [3,4], obtaining natural contrast due to the different absorption of carbon and oxygen, limiting such range. High production of energetic EUV and SXR radiation, which represents a fundamental requirement for microscopy, can be obtained by choosing sources and optics capable of reaching a high photon flux [5,6]. Different types of optics were employed in the last 30 years for X-ray imaging experiments, from reflective optics, such as multilayer mirrors [7], Kirkpatrick–Baez mirrors [8], and compound refractive lenses [9] to diffractive optics, such as multilayer Laue lenses [10] and, particularly, Fresnel zone plate optics (FZPs) [11,12]. Moreover, large facilities, such as X-ray free electron lasers (XFELs) [13] and synchrotrons [14,15] were improved, although they require high maintenance costs because of their complexity. In the last two decades, considerable efforts were made to develop compact EUV and SXR sources to be used in compact, cheaper, and user-friendly laboratory systems.

Short EUV radiation can be employed to get information about thin samples due to their high absorption by solid thin materials (thicknesses of the order of ~100 nm) and by gaseous materials (few millimeters thick) [16]. Moreover, this radiation enables to analyze micro-cracks into nanostructures [17], to visualize the gas flow in two-dimensional (2D) [18] and three-dimensional (3D) mode [19], usually investigated with indirect techniques, such as the interferometry [20], or for high-resolution lithography, reaching sub-7 nm patterning at 13.5 nm [21].

Different types of compact EUV sources currently allow acquiring images with a sub-micrometer resolution. Employing a recombination laser at λ = 18.2 nm, a 700 nm half-pitch spatial resolution was obtained [22]. Radiation from a capillary discharge laser operating at a wavelength of λ = 46.9 nm allowed to obtain a spatial resolution lower than 150 nm [23], down to ~50 nm [24], and holographic images down to sub-50 nm [25]. However, the number of acquired images is limited by the relatively short lifetime of the capillaries [26]. A transmission microscope, based on a Ni-like Cd-EUV laser operating at 13.2 nm wavelength, is capable to achieve a sub-38 nm spatial resolution in a picosecond [27]. Gas-plasma sources can be optimized to obtain high-resolution imaging employing different techniques, such as supersonic jets [28], high order harmonic generation (HHG) [29], and laser-plasma sources [30].

Short wavelength microscopy investigations can be extended, employing, also, radiation from the SXR range. Full field X-ray microscopy is typically limited by the low transmission efficiency of the diffractive FZPs employed. This obstacle can be overtaken by developing bright sources, such as spatially coherent plasma-based X-ray lasers (XRLs) [31] or HHG [32], which lead the possibilities to obtain high-resolution images with lensless techniques, such as coherent diffractive imaging (CDI) [33], holography [34], and ptychography [35]. Although such techniques avoid dealing with the geometrical factors of the lenses (which main constraints are represented by aberrations, small penetration length, and depth of focus in the SXR range), the employed sources are quite complex and expensive, achieving outstanding results, mainly in the EUV [36] and hard X-ray [37] range, but not in the "water-window", where a lower photon flux is obtained. Hence, there is a need to develop compact and user friendly sources that enable the possibility to carry out imaging experiments in university laboratories, with remarkable results. A recently developed droplet-based SXR source operating at λ = 3.37 nm allowed to acquire images with a spatial resolution of ~40 nm [38]. A gas-discharge source employing He-like N_2 emission reached a 40 nm spatial resolution at up to 1 kHz source repetition rate [39]. A liquid N_2-based SXR source at λ = 2.48 nm was employed to demonstrate a compact full field transmission microscope capable to acquire images of biological samples, with a half-pitch spatial resolution of 50 nm and 1 min exposure [40]. Similar sources were also employed to demonstrate laboratory "water window" X-ray microscopy of cryo-frozen biological samples approaching a ~40 nm spatial resolution in a very short exposure time (10 s) and at a 2 kHz repetition rate [41]. However, the mentioned sources are complicated to use and the setup may occupy a quite large area, limiting their versatility and usability. One of the newer compact developed microscopes, which employs a single gas stream jet, even if simple in construction, has the limitation of acquiring images achieving a resolution

of ~100 nm, with an exposure time up to 1–2 h [42]. As it is possible to understand from these few examples, a compromise always has to be found between the size and the versatility of laboratories' compact sources. The 2D imaging techniques are limited in the depth of field, resulting often in the loss of sample details, which are visible only applying a 3D tomographic method.

SXR radiation can be employed for tomography, by combining and reconstructing several 2D projections of the same sample, acquired at different angles. Tomographic high-resolution imaging was performed in the "water window" spectral range pushing the resolution limit up to 11 nm for inorganic samples [43] and from 25 to 60 nm for biological samples, exploiting internal cellular structures employing cryo-equipment [44–46]. This new imaging approach has to deal with several technical problems, one of the main consisting of the possibility to acquire images of biological samples before their degradation [47], which, nowadays, can be overcome employing intense pulses from large facilities, such as XFELs [48]. Technological advancements lead to the development of laboratory-compact sources for high-resolution imaging, operating in short wavelengths. In this regard, laser-plasma sources based on a double stream gas-puff target presents several advantages. Employing a high repetition rate laser, such a source can be used continuously, obtaining high photon flux even with a monochromatic radiation emission. The gas-puff target provides an optimal medium with an adequate density profile for the creation of the plasma emitting EUV/SXR radiation, which results twice of that obtainable with a single gas jet, i.e., ≥12 mg/cc [49]. This ensures a better control over the density, minimizing gradients in the plasma. Moreover, dealing with gases, the source is "debris free", since no ablation is produced during the plasma formation, comparing to solid target sources. This last peculiarity offers the possibility to generate the plasma efficiently and to have tens of thousands of shots per day. Finally, the emission spectrum can be easily modified by changing the gas target or tuning the emission by applying appropriate thin film filters. The double gas jet allows to obtain sufficient plasma density and, thus, enough photon flux to acquire microscopy images. Despite its simple construction it is robust and has a low maintenance costs. The double stream gas-puff target source represents a versatile alternative to perform experiments in small academic laboratories without the necessity to access to large-scale facilities, and can be regarded as complementary diagnostic tools for high spatial resolution imaging, obtaining additional information about the objects not directly available using other microscopy techniques. The laser-plasma source based on a double stream gas-puff target was successfully employed, thus far, for different applications [50], such as for shadowgraphy systems [51], radiography [52], radiobiology [53], photoionization [54], metrology [55], plasma channel studies [56] and, as will be shown extensively, imaging experiments [57–59].

Full field microscopy based on gas-puff target sources and diffractive optics, such as FZPs, represents a good way to perform experiments on small scales, obtaining a sub-100 nm resolution [58,60]. Moreover, it is based on a compact and accessible setup, opening the possibility for wider multidisciplinary collaboration with biologists, chemists, and scientists from other disciplines. Despite the employed FZPs allow achieving a sub-10 nm spatial resolution [61], it is still challenging to find a necessary compromise between the exposure time and the size and complexity of the microscope's architecture [42]. Several parameters can be improved to overcome this trade-off, such as obtaining high photon flux and repetition rate minimizing the debris production, increasing the charge-coupled device (CCD) resolution [62], etc.

The gas-puff target source can also be successfully employed for the so-called soft X-rays contact microscopy, enabling to achieve a good contrast image of wet biological samples up to several μm thick [63], and avoiding complex and required invasive preparation procedures of the samples, such as the dehydration process, necessary for scanning electron microscopy and the immunofluorescence labeling method needed for fluorescent microscopy [64,65]. Ultra-short SXR pulse radiations generated by laser-produced plasma sources make it possible to acquire 10 nm resolution images of living biological samples before the occurrence of the sample damage [66], employing the natural contrast of the "water window" spectral range [63]. The double stream gas-puff target represents an excellent

source to acquire contrast images in this wavelength range and can be successfully employed for contact microscopy of biological samples, achieving a half-pitch spatial resolution of about 80 nm [67].

The following review is directed toward the development of microscopes based on gas-puff target sources emitting in the EUV and SXR spectral range, presenting several biological imaged samples. It will be shown that such microscopes allow achieving a sub-100 nm spatial resolution, superior to the classical visible light microscopes. The development of such microscopes provides the opportunity for imaging of various samples and for identifying additional information about them, which cannot be directly observed using other imaging methods.

2. Materials and Methods—Double Stream Gas-Puff Target Source Description

Although if a gaseous laser-plasma source based on a single stream of gas-puff target allows to overpass the problem of debris production observed employing solid targets, it presents the disadvantage of the high divergence of the injected gas from the nozzle to the vacuum and the consequent insufficient gas density, away from the nozzle, limiting efficient EUV/SXR radiation emission. This issue can be solved by employing a double stream gas-puff target system, developed at the Institute of Optoelectronics, Military University of Technology (MUT) in the early 2000s [68]. The target is formed by the injection of gas under high pressure from a nozzle into a low-Z gas cloud, surrounding the nozzle output. The surrounding gas directs the gas flowing through the nozzle, preventing its quasi-spherical expansion. In this way, it is possible to form an elongated gas jet with a high density even at a relatively long distance from the nozzle [49–69]. The laser-plasma source based on a double stream gas-puff target consists of two coaxial nozzles, a ring-shaped outer nozzle with an inner diameter of 0.7 mm, and an outer diameter of 1.5 mm to create a hollow stream of gas formed by injection of low-Z gas (He) surrounding the inner nozzle. It consists of a circular orifice, a 0.4 mm diameter, supplied with the high-Z working gas (generally, N_2 gas jet for SXR microscopy and Ar gas jet for EUV microscopy). The hollow low-Z stream of gas injected through the outer nozzle confines the high-Z gas flowing through the inner nozzle, and subsequently prevents the diverging of the working gas flow outside the central nozzle. The distance from the nozzle to the focus of the laser beam cannot be too large, to maintain the working gas density at an optimal level, otherwise causing reduction of photon production and cannot be too small because the plasma, after hundreds of hours of source operation at 10 Hz repetition rate, will degrade the nozzle's surface. To get the highest photon flux achievable for imaging experiments, it is important to set the right gas pressures and synchronize the gas-puff emission with the laser pulses [70].

2.1. Pressure Optimization

Two working gases (in our case Ar and N_2) have been used to form the gas-puff target. These gases have been demonstrated to give emission in the "water window" soft X-ray and the EUV spectral ranges, respectively, with different laser systems and for different applications. The outer gas pressure reduces the working gas density gradient along the nozzle axis, which makes it possible to obtain higher working gas density further away from the nozzle, improving the EUV/SXR emission yield and avoiding nozzle ablation by repetitive plasma formation. Thus, for optimal performance, the pressures of each gas are needed to be found to ensure the achievement of the highest possible photon flux in the image plane at the CCD camera. The gases are injected through the nozzles driven by a separate electromagnetic stainless steel valve system. The electromagnetic valve (Figure 1a) is driven by electric pulses synchronously with the laser driving pulse and can operate at a repetition rate of up to 30 Hz. A 3D scheme and a photo of the double stream gas-puff target source placed inside a vacuum chamber are shown in Figure 1b,c, respectively.
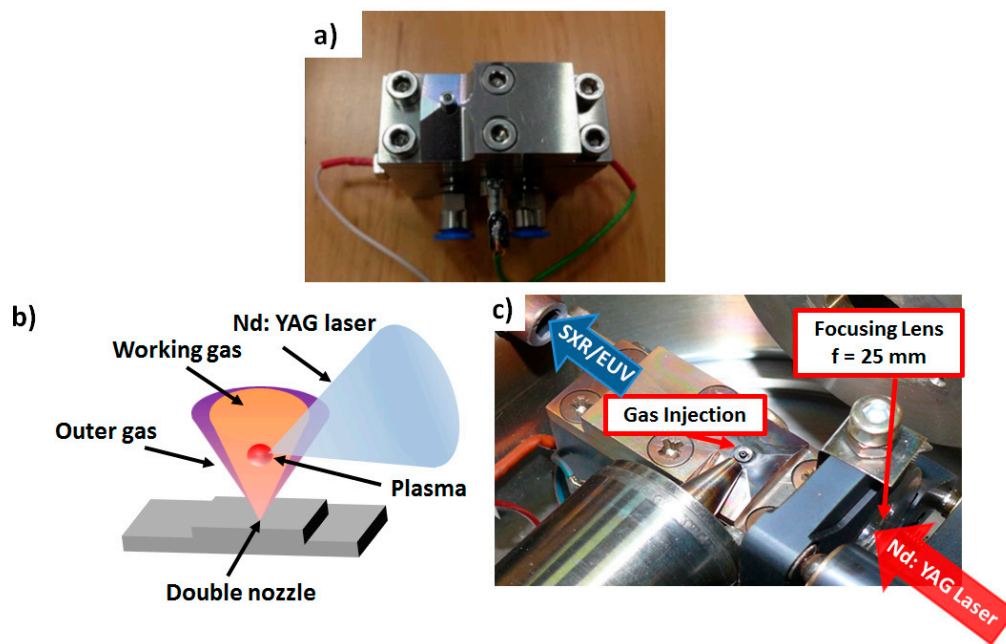
Figure 1. (**a**) Photo of the valve producing a double stream gas-puff target. (**b**) Shows a three-dimensional (3D) scheme of the gas-puff target irradiated with an Nd:YAG laser. (**c**) Shows the gas-puff target located inside the vacuum chamber.

2.2. Time Synchronization

The EUV/SXR radiation is efficiently generated thanks to appropriate time synchronization between the gas-puff target formation and the arrival of the laser beam. The jitter in the valve time sequence can be minimized by synchronizing a valve controller with a synchronization output of the pumping laser. As the system works at a 10 Hz repetition rate, the duration of one cycle was 100 ms. Two times are defining the time sequence for each valve. The Time Delay (TD) defines the delay between the synchronizing pulse, generated at 1 ms before the laser pulse and the time of the valve opening, while the Pulse Width (PW) determines the time for which the valve must be opened. TD and PW have to be properly optimized so that valve and nozzles can operate continuously, for hundreds of thousands of laser pulses, without being damaged. A scheme of the delay timings and pulse durations triggered by the laser is presented in Figure 2.
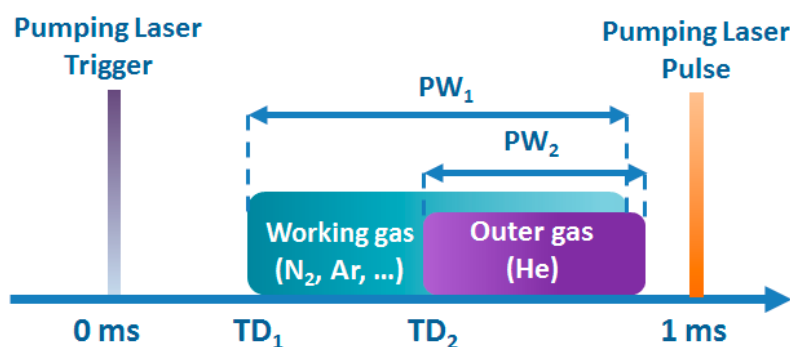

Figure 2. Scheme of the delay timing setting for the laser-plasma source based on a double stream gas-puff target. Figure modified, based on [70].

The source can be monochromatized, and offers the possibility to quickly change the emission spectrum by changing the gases and filters. Depending on the spectral emission needed, different gasses are supplied to the inner nozzle, to achieve efficient emission in the extreme ultraviolet (Ar, Xe) and/or

in the soft X-ray region (N_2, Kr, Ar). The plasma emission can be spectrally narrowed, to obtain quasi-monochromatic radiation. To achieve that, the experimental system was equipped with a series of thin film filters and/or a multilayer mirror for narrowing the spectral emission from a laser-produced plasma, according to the online database CXRO [16].

3. EUV and SXR Full Field Microscopes Based on a Double Stream Gas-Puff Target Source

3.1. Full Field EUV Microscope

The recently developed EUV microscope (scheme and picture are shown in Figure 3a,b) [71], having a total volume of (W × D × H) 100 cm × 70 cm × 161 cm, represents one of the most compact microscopes reported in the literature and was developed as a technological demonstrator, based on similar experimental systems [72].
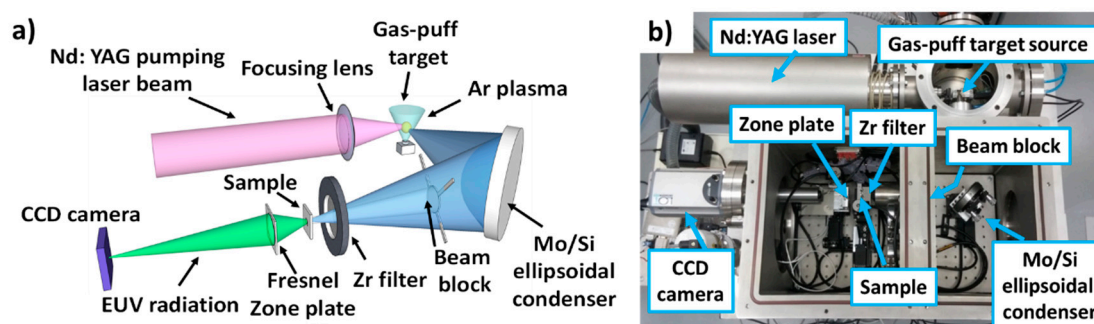
Figure 3. (**a**) Scheme and (**b**) external view of the extreme ultraviolet (EUV) microscope. Figure modified, based on [71].

An infrared Nd:YAG laser NL 302 from Eksma, Vilnius, Lithuania (λ = 1064 nm, 500 mJ energy, 4 ns time pulse duration, and intensity of 10^{11} W/cm^2), was focused using a proper lens (f = 25 mm) onto a double stream gas-puff target. The Ar plasma radiation, at the wavelength of 13.5 ± 0.5 nm, was spectrally narrowed by an ellipsoidal off-axis mirror, coated with a Mo/Si multilayer mirror (MLM), having the function of condenser, reflecting the EUV radiation at 45° incidence angle. The longer wavelengths emitted from the Ar plasma (λ > 16 nm) have been cut employing a free standing 250 nm thick Zr filter (Lebow, CA, USA). The sample was imaged using an FZP objective onto the CCD camera. The system is equipped with differential pumping, which allows avoiding high gas pressure inside the vacuum chamber. During the test phases, a pressure of ~10^{-4} mbar was constantly maintained by using two scroll pumps and one turbo-molecular pump. The pressure inside the source chamber (of a few mbar during the source operation) was separated from the pressure inside the microscope chamber (where it is possible to achieve a pressure down to 10^{-5} mbar) by using a cone-shaped differential pumping aperture (1 mm in diameter). The object was locked in place by a magnetic holder (KB25/M, from Thorlabs Inc., Newton, NJ, USA), and its position was finely adjusted using three-axis motorized translation stages, (8MT173-20 from Standa, Lithuania), having a position accuracy of 1.25 μm. A dedicated piezo-stage (LPS-45 from PI miCos GmbH, Eschbach, Germany), with a repeatability of 50 nm, was used for accurate positioning of the FZP along the optical axis. The chamber was equipped with a supplementary load lock, to easily replace the sample. The gas pressure was adjusted to obtain the highest photon flux in the focal plane of the condenser. Ar (working gas) pressure was set to 10 bar, and He (outer gas) pressure was set to 6 bar. To avoid nozzles damaging by the plasma generation, the focal spot was located 1.5 mm away from the nozzle plane. The time delays between the synchronization pulse from the pumping laser power supply and the opening times of the two valves supplying the nozzles (with Ar and He) were 100 μs and 230 μs, respectively, while the pulse width was 500 μs for both valves. Finally, the time between the synchronization pulse and the laser pulse generation was set to 1 ms.

3.1.1. EUV Source Spectral Distribution and Photon Flux Estimation

Spectral measurements were performed using a silicon nitride (Si_3N_4) transmission grating spectrometer (200 nm period, 5000 lines/mm) and acquired by a CCD camera X-vision (from Reflex s.r.o., Prague, Czech Republic) with an exposure of 20 EUV pulses. Figure 4 shows the obtained spectrum from Ar plasma source, acquired directly in a wavelength range of 6–16 nm and employing a 250 nm thick Zr filter (continue-blue line). The transmission curve for the MLM condenser is depicted as a dashed-orange line, while the contribution in the 13–14 nm EUV spectral range, focused and reflected from the multilayer mirror (MLM) and employed for microscopy, is depicted as a purple, dash-dotted line. The main spectral lines for Ar^{VIII} emission, are $2p^63p$-$2p^65d$ at $\lambda = 13.79$ nm and $2p^63s$-$2p^65p$ at $\lambda = 13.84$ nm [73], which is predominant in the $\Delta\lambda = 1$ nm MLM transmission band. However, the spectrometer spectral resolution, of 0.51 Å, was not enough to allow us to resolve such closely spaced lines.
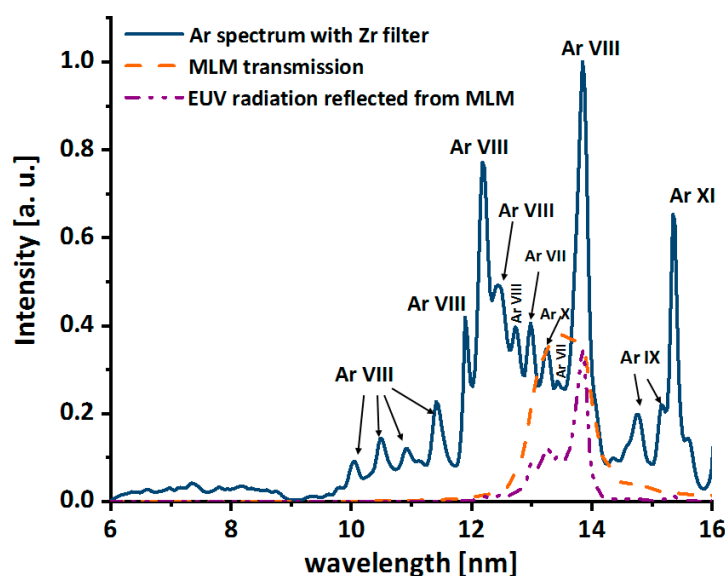

Figure 4. The spectrum of the Ar plasma emission (blue line) acquired with 20 EUV pulses and filtered using a 250 nm thick Zr filter. Radiation from the plasma was focused using the multilayer condenser mirror, which transmission is shown in orange, dashed line. The total contribution in the wavelength range 13–14 nm, used for imaging experiments, is shown as a purple, dash-dotted line. Figure modified, based on [58].

The photon emission of the EUV source was estimated using a commercial AXUV 100 silicon p-n junction photodiode (from, IRD Inc., California, USA) detector, active area 10×10 mm^2, whose signal was stored using a 4 GHz Tektronix Inc. (Beaverton, OR, USA), DPO 70404 oscilloscope. The photon flux estimated for a single EUV pulse, in the considered range of 13–14 nm, was $(1.36 \pm 0.07) \times 10^{11}$ photons/pulse, corresponding to an energy of ~1.9 mJ/pulse.

3.1.2. EUV Source Plasma Size Estimation

The EUV plasma size was estimated using a pinhole camera (pinhole diameter of 33 µm), at a distance of 365 mm from the laser-plasma. The CCD camera was set at 520 mm from the pinhole, resulting in a geometrical ratio of 1.42× camera magnification. A 250 nm Zr filter, placed at a distance of 100 mm from the pinhole, allowed to select of the EUV radiation. The EUV plasma size, measured as full-width-half-maximum (FWHM) profile in the two orthogonal directions (H × V) was 0.75×0.38 mm^2, as it is shown in Figure 5a,b [58].
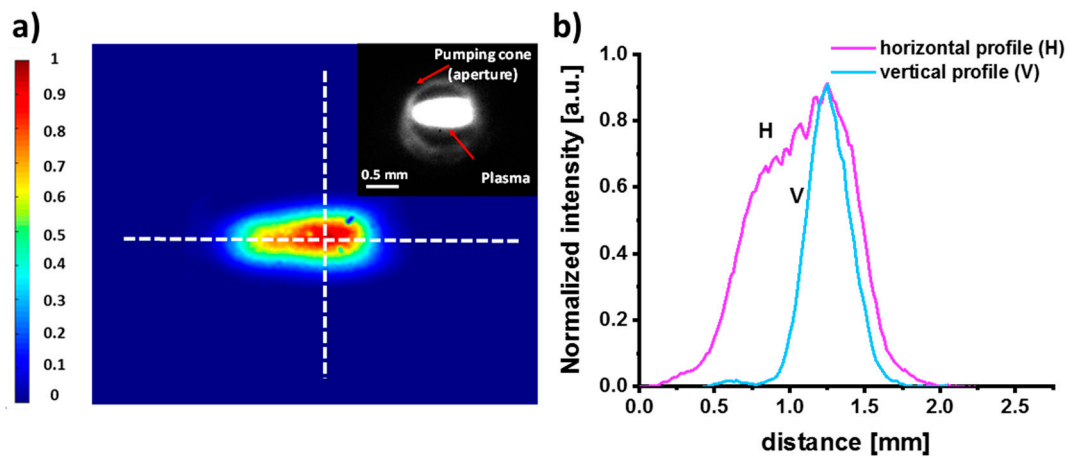
Figure 5. (**a**) Plasma profile in false colors, showing the most intense region of plasma emitting EUV radiation (red). The inset shows the Ar plasma image obtained with a pinhole camera. (**b**) Shows the EUV emission spectrum (H × V) from Ar plasma generated by focusing Nd:YAG laser pulses irradiating a double stream gas-puff target. Figure modified, based on [58].

3.1.3. Fresnel Zone Plate for EUV Microscopy

The employed FZP by Zone Plates Ltd. (London, UK), having a diameter $D_{FZP} = 200$ μm, number of zones $N_{FZP} = 1000$ and outer zone width $\Delta r = 50$ nm, made by electron beam lithography in a 200 nm thick polymethyl methacrylate (PMMA) layer spin-coated on top of a 50 nm thick Si_3N_4 membrane, resulting in first order diffraction efficiency of ~20%. The theoretical spatial resolution is 61 nm and the depth of focus (DOF) ± 369 nm. The match of the numerical aperture of the condenser ($NA_{\_CH} = 0.11$ in horizontal and $NA_{\_CV} = 0.15$ in the vertical direction) with the numerical aperture of the FZP objective ($NA_{\_FZP} = 0.137$) guarantees the spatial incoherent object illumination [74]. The geometrical magnification (at a distance FZP to CCD of 28.1 cm) was 410×. The radiation emitted from the Ar plasma was collected and spectrally narrowed down by the ellipsoidal multilayer mirror, located at a distance of 254 mm from the plasma. The condenser reflects radiation at the wavelength of 13.5 ± 0.5 nm (FWHM), with an optimized curvature to minimize the spherical aberrations at the incidence angle of 45°. An ellipsoidal silica mirror (Reflex s.r.o., Prague, Czech Republic), 80 mm in diameter (radii of 179.6 mm and 254 mm in two orthogonal directions), was used as a substrate for the deposition of the Mo/Si multilayers (made at the Fraunhofer Institute for Applied Optics and Precision Engineering IOF, Jena, Germany). Thus, the plasma was imaged by the condenser with a magnification of M = 1. The quasi-monochromatic EUV radiation was produced and focused at the sample plane, corresponding to the second focal plane of the condenser, ensuring the maximum energy and uniform spatial distribution of the illumination on the sample surface, within the field of view (FOV) of the microscope. To absorb the stray EUV radiation through the FZP, a circular beam stop made from a 0.3 mm thick Al sheet (diameter of 3.2 mm) was placed 20 cm downstream of the condenser. The smallest achievable spot was ellipsoidal, horizontally elongated, having an FWHM of 1.5×0.8 mm^2.

3.1.4. EUV Full Field Imaging of Test Objects and Spatial Resolution Estimation

As the first test sample, a 10 μm TEM copper mesh (SPI supplies, West Chester, PA, USA), a period of 12.5 μm, square holes with sizes of 7.5×7.5 μm^2 and 5 mm width bars, was imaged (Figure 6a,b). Such a well-defined structure provided a total photons absorption in the surface and the total transmission in the mesh holes, resulting in good optical contrast. The image, shown in Figure 6a, was acquired by a scanning electron microscope (SEM, FEI, 3D FEG, Hillsboro, OR, USA), while Figure 6b was obtained with a time integration of 200 EUV pulses at a 10 Hz repetition rate, corresponding to an exposure time of 20 s, and acquired using an i-Kon M CCD camera (from Andor,

Belfast, UK), cooled to −20°C, with a readout set to 50 kHz, in order to minimize the read noise. The contrasts of Figure 6a,b, are reversed because the bright areas in the SEM image were obtained from backscattered electrons from the test mesh, while the light areas in the EUV microscope image (holes) are formed by photons transmitted through the holes in the mesh at the wavelength of 13.84 nm. The spatial resolution of the microscope was assessed by applying the knife-edge (KE) test [1], in the dashed line depicted in Figure 6b. The KE test was applied in a 2 μm line, corresponding to ~61 pixels in the EUV image. It results in a single-pixel size of 33 nm while the field of view (FOV) of the EUV image was ~34 × 34 μm^2 in size. The KE was calculated in a 10–90% intensity change over a distance 3 pixels, corresponding to 95 nm, i.e., to a half-pitch spatial resolution of 48 nm (Figure 6c), which is almost one order of magnitude better than the obtainable resolution using a full field visible light microscopes, which is limited by a wavelength to 300 nm [58].
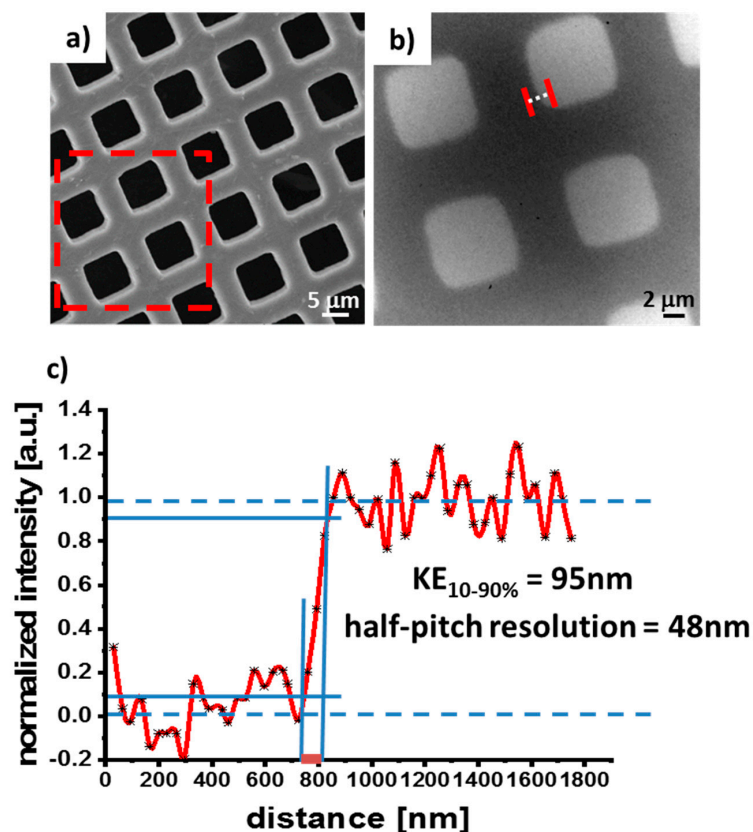
Figure 6. (**a**) SEM and (**b**) EUV images of the copper mesh used as a test sample. In (**c**) is shown the knife-edge (KE) test (estimated on the dashed line indicated in (**b**)) to calculate the half-pitch spatial resolution of the microscope, which results in 48 nm. Figure modified, based on [58].

Such estimation shows that the obtained resolution is 60% larger than the expected diffraction limit, which, according to the Rayleigh resolution, is 1.22Δr~60 nm. This discrepancy depends on the outer zones of the zone plate, fabricated with a zone width-to-depth ratio equal to 4, in a 200 nm thick PMMA layer. Moreover, it has to be taken into account that the zone plate is a dispersive diffractive element and that the considered EUV radiation is not strictly monochromatic and the presence of other spectral components, although weak comparing to the dominating 3s-5d Ar^{7+} line, affects the quality of the acquired image.

3.2. Full Field SXR Microscope

A scheme and a picture of the SXR "water window" microscope system, located in a single optical table (1.8 × 1.2 m^2) are depicted in Figure 7a,b, while Figure 7c shows the optical components.

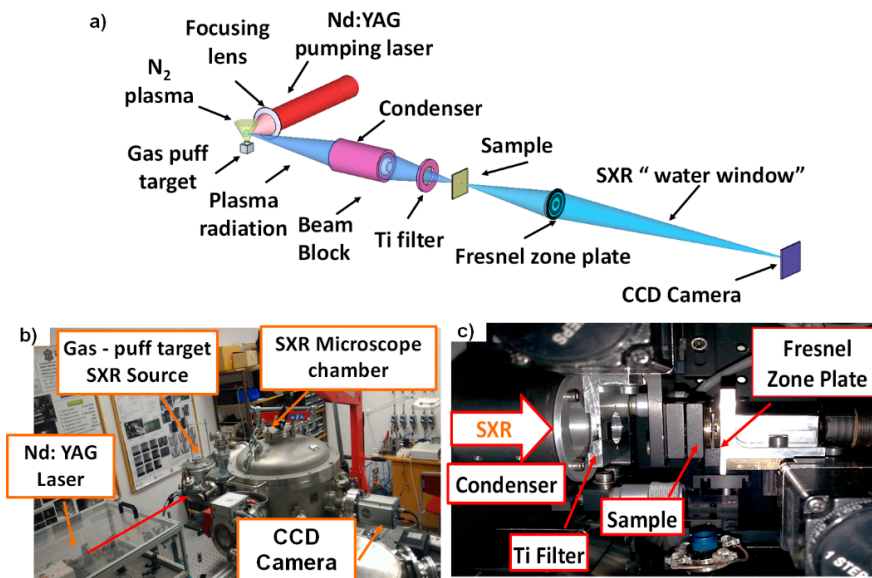**Figure 7.** (**a**) Scheme and (**b**) overall view of the "water window" microscope. In (**c**) are shown the internal optical components of the microscope [75,76].

The N_2 plasma was produced by focusing an infrared Nd:YAG pulsed laser NL303HT from EKSPLA (Vilnius, Lithuania), operating at $\lambda = 1064$ nm, with a pulse duration of 4 ns and energy of 0.74 J at 1–10 Hz repetition rate, onto a double stream gas-puff target. The focal point to the nozzle was set to 1.5 mm, to avoid nozzle damage by plasma formation. The SXR radiation from the plasma was efficiently focused by an ellipsoidal axisymmetric SXR condenser onto the object. A Si_3N_4 FZP objective was used to magnify the image of the sample onto a back-illuminated SXR-sensitive CCD camera. The SXR spectrum obtained was measured using a transmission grating spectrometer (with a free standing grating, 5000 lines/mm, 33 μm entrance slit) and an i-Kon CCD camera. The inverse relative bandwidth of the spectrometer, estimated from the spectrum, was $\lambda/\Delta\lambda \sim 70$ at $\lambda = 2.88$ nm wavelength. Figure 8 shows the unfiltered N_2 emission spectrum (black line), which mainly consists of two peaks, i.e., the N^{5+}: $1s^2$-$1s^2p$ He-like N_2 line at $\lambda = 2.88$ nm and the N^{6+}: $1s$-$2p$ H-like N_2 line at $\lambda = 2.478$ nm, which are in the "water window" spectral range, according to [73]. The 200 nm thick L-α Ti edge at $\lambda \sim 2.7$ nm filter (blue line) cuts off the H-like line almost completely, in order to use the quasi-monochromatic N_2 emission at 2.88 nm for imaging experiments.
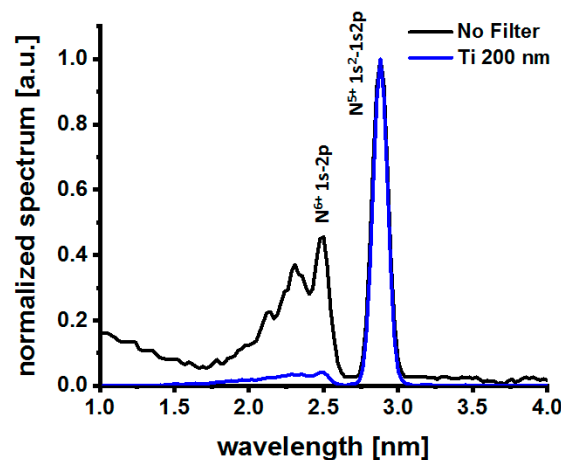

Figure 8. N_2 plasma emission in the "water window" spectral range, unfiltered (black line) and filtered with a 200 nm thick Ti filter (blue line).

3.2.1. SXR Source Spectral Distribution and Photon Flux Estimation

The source photon flux was measured at the sample plane using an AXUV 100 photodiode. The broad spectral emission from the plasma was filtered placing a 200 nm Ti filter 31cm from the detector. The acquired photon flux, at 2.88 nm wavelength, was equal to $(7.9 \pm 0.2) \times 10^9$ photons/pulse, corresponding to an energy of ~561 nJ/pulse. Even in this case, the focal point–nozzle distance was set to 1.5 mm, to avoid nozzle damage by repeatable plasma formation. The working gas (N_2), was injected by the inner gas with a time delay of 400 μs after the arrival of synchronization pulse from the laser power supply and stays open for a time of 350 μs. The outer nozzle, injecting He, which will open 500 μs after the arrival of the synchronization pulse, remains open for the next 250 μs. Subsequently, a laser pulse producing, in turn, an N_2/He gas-puff target is generated. The N_2 plasma produced by the gas-puff target emits the SXR radiation, employed for imaging experiments.

3.2.2. SXR Source Plasma Size Estimation

Moreover, in this case, using a pinhole camera it was possible to obtain the N_2 plasma size in the "water window" spectral range, which FWHM resulted to be 0.47×0.31 mm^2. The plasma profile (in false colors) and its distribution are shown in Figure 9a,b, respectively [75,77].
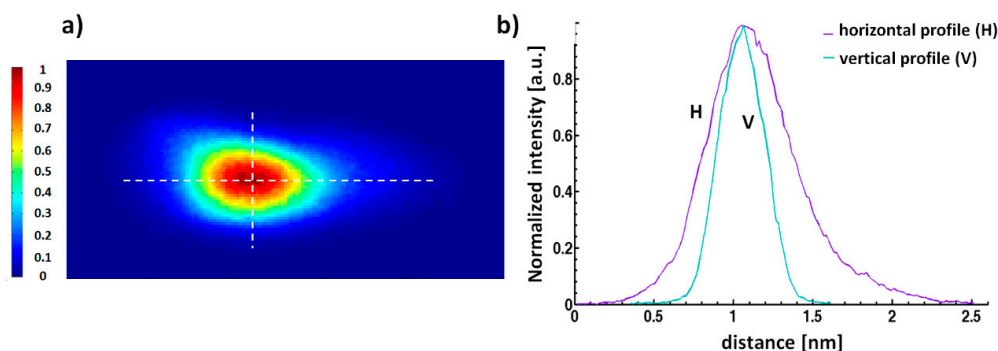

Figure 9. (**a**) Plasma profile in false colors, showing the most intense region of plasma emitting soft X-ray (SXR) radiation. (**b**) Shows the SXR emission spectrum (H × V) obtained in the "water window" spectral range from N_2 plasma generated by focusing Nd:YAG laser pulses irradiating a double stream gas-puff target. Figure modified, based on [75].

3.2.3. Fresnel Zone Plate for SXR Microscopy

The 400 nm thick Si_3N_4 FZP (by ZonePlates Ltd., London, UK) employed for SXR imaging in the "water window" spectral range has a 250 μm diameter, 30 nm outer zone width, and focal length, at λ = 2.88 nm, of 2.6 mm. The image plane was located 574 mm from the zone plate. Thus, the geometrical magnification of the system was ~220×. The cross section of the employed lens has a rectangular profile. Thus, if the main light loss in the lens comes from the absorption of electromagnetic radiation from the zones (~50%), it is necessary to take into account also the higher orders of diffraction in which part of the energy is distributed. It is, however, possible to realize these lenses in a thin layer of material in order that their diffraction efficiency employing SXR radiation is ~20% with respect to the zero diffraction order.

An ellipsoidal, axisymmetric, nickel-coated condenser mirror, manufactured by Rigaku Innovative Technologies (Prague, Czech Republic), was employed to collect the SXR radiation. The condenser efficiently reflects radiation from the SXR region focusing this radiation on the sample plane, with a cut off energy of ~800 eV (~1.5 nm critical wavelength), above Kα-O edge (E = 543 eV). As a result, it is possible to reflect the SXR radiation at a small angle. The condenser was mounted on a three-axis (xyz) motorized translation stage, enabling a fine adjustment of the position, while a manual stage permits to change the tilt angle in two directions. The distance source-condenser was 60 mm, while the distance condenser-sample was 140 mm. The entrance and exit diameters of the condenser were equal

to 11.7 and 14 mm, respectively. It results in an entrance numerical aperture of N_{AC_in} = 0.09 and an exit numerical aperture of N_{AC_out} = 0.05, respectively. This proves incoherent illumination, since σ = N_{AC_out}/NA_{FZP} = ~1 [78], limiting the loss of photons. The condenser alignment is a very delicate operation, since, depending on the sample illumination pattern, allows to enhance or diminish selected spatial frequencies at radial distances in the image plane. The alignment was performed by a direct projection of the condenser illumination pattern onto the CCD detector.

3.2.4. SXR Full Field Imaging of Test Objects and Spatial Resolution Estimation

As for the EUV system, the SXR microscope's spatial resolution was estimated imaging a copper, 2000 periods per inch TEM mesh (SPI supplies, PA, USA). The image depicted in Figure 10a was acquired first using an optical microscope (objective with NA = 0.7 and diffraction limit of ~420 nm). After having set the CCD camera with the optimal parameters to improve the signal-to-noise (SNR) ratio [79], the test sample was imaged in the "water window" spectral range, with 100 SXR pulses and a 10 s exposure time using a GE 2048-2048 BI camera (greateyes GmbH, Berlin, Germany), 2048 × 2048 pixels, pixel size 13.5 μm × 13.5 μm, as shown in Figure 10b. In the same figure, some imperfections of the mesh are magnified, including ~200 nm wide features. The DOF of the objective was equal to ±1.25 μm. The microscope resolution was assessed by the knife-edge test applied in the region indicated with a white-dotted line in Figure 10b. The KE test result (Figure 10c) shows that 10–90% intensity transition in the normalized lineout was ~120 nm (Rayleigh resolution), resulting in a half-pitch spatial resolution of ~60 nm [80].
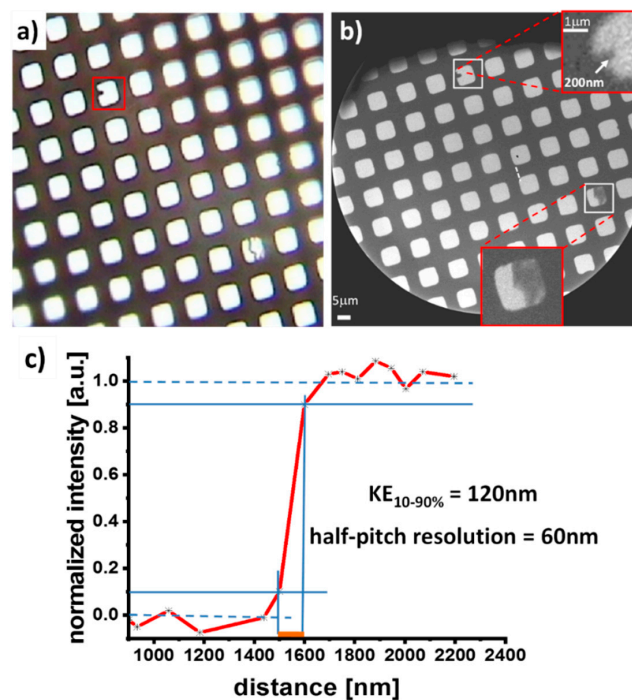

Figure 10. (**a**) Optical and (**b**) SXR image of a #2000 TEM copper mesh. Insets in (**b**) shows some defects, including ~200 nm wide features. (**c**) Shows the knife-edge test, performed on the base of the white-dotted line in (**b**). Figure modified, based on [80].

3.3. SXR Tomography and 3D Imaging

The SXR equipment was later improved in order to acquire 3D images, i.e., topography of the samples [59]. An Nd:YAG (YG981, from Quantel, MT, USA), with a pulse duration of 8 ns, 20 Hz repetition rate, and an energy of 1.5 J was employed. The photon flux of the source, at the sample plane, was of ~9×10^9 photons/pulse at 2.88 nm wavelength. The experimental setup is depicted in Figure 11a, while the internal components of the microscope are shown in Figure 11b. The system was

equipped with a piezoelectric translation stage (Q-545.240, travel range of 26 mm, 1 nm resolution, and bidirectional repeatability of ±18 nm) and a rotation stage (Q-632.930, rotation range >360°, 0.75 μrad sensor resolution, and unidirectional repeatability 6 μrad), from Pi miCos, to move the sample to observe with nanometric precision. Thus, according to the type of sample to observe, two different sample holders, machined ad hoc, can be mounted inside the chamber: a tip-holder (Figure 11c), on the top of which it is possible to place samples in granular form, and a slit-holder (Figure 11d), having a width of 0.21 mm and a depth of 1 mm, which can host a standard TEM Si_3N_4 membrane (typically 30 nm thick), on the top of which are typically deposited a few drops of a liquid sample [59]. The slit-holder, having a slot 0.5 mm deep and 0.5 mm wide, ensures that the Si_3N_4 membrane can be visible for a large range of rotation angles. The rotation angles range is limited to the geometry of the holder, ±60° from normal incidence illumination. The holders are positioned on a rotation stage and the rotation axis of the sample is located 140 mm from the condenser exit plane, in its focal point. To avoid eccentricity, for both the holders, it is required an accurate alignment of their rotation axis with the rotation axis of the stage.
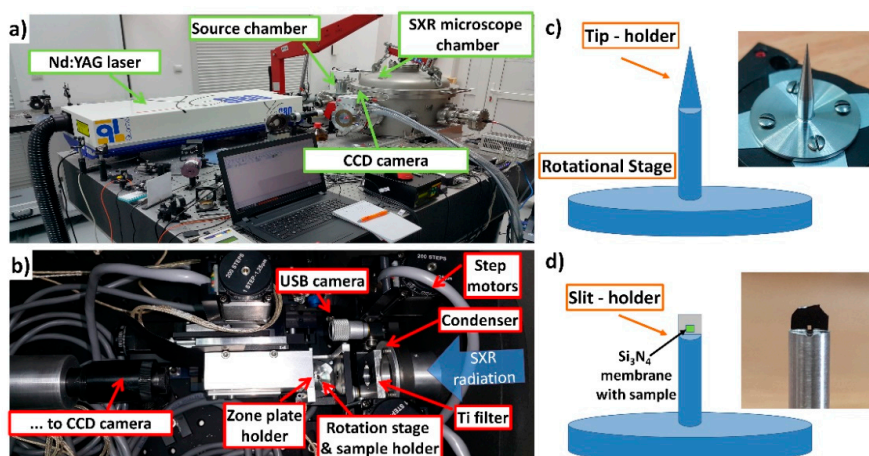

Figure 11. (**a**) SXR tomography setup and (**b**) internal components of the microscope. In (**c**,**d**) a scheme and a picture of the tip- and slit-holder are depicted, respectively. Figure modified, based on [59].

The projections acquisition was optimized cooling down the CCD camera at a temperature of −20 °C, in order to reduce its internal noise and to improve the SNR of the acquired images. The tomography system consents to acquire the projections using two different CCD cameras, inside or outside the microscopy chamber. An Andor i-Kon, DX-420-BN camera, 256 × 1024 pixels (25 × 25 μm^2 pixel size) can be placed inside the microscope vacuum chamber at a distance of ~270 mm from the FZP, resulting in a (geometric) magnification of ~100× (sample—CCD camera). Alternatively, a second camera, Andor i-Kon, DO-934N-BN, 1024 × 1024 pixels (13 × 13 μm^2 pixel size), can be located externally to the microscope vacuum chamber, at a distance of 530 mm from the FZP, resulting in a magnification of ~200×. In this second case, the resulting FOV is 60 × 60 μm^2, while the spatial resolution is ~60 nm [59]. The employment of the internal CCD camera, instead, limits horizontally the FOV, resulting in 150 × 60 μm^2; however, the spatial resolution of the 2D projections is limited by the detector sampling to ~250 nm. Even though the external camera allows the acquisition of 2D projections with higher resolution and magnification, the use of the internal camera results easier and more useful for imaging of the samples whose axis of rotation is unknown, and must be determined by rotating the sample several times, compensating for the offset, according to its distribution.

3.4. SXR Contact Microscope

The microscope described in this section is based on the same principle of the full field SXR setup, with the difference that the source is based on Ar plasma. In such a system, the Ar ionization is enough

to emit radiation in the "water window" spectral range. The samples are placed in contact with a 500 nm thick PMMA photoresist, deposited onto a silicon wafer, which acts as a detector to record the images of the samples. The photoresist irradiation by SXR and its subsequent chemical development causes local modification of the structure. The X-ray irradiation energy absorbed by the photoresist is converted into a relief-like structure, where the height difference will be directly proportional to the deposited radiation dose. Such difference is afterward converted to an image, typically by atomic force microscope (AFM).

The system, firstly developed for imaging of dried samples [67], was then optimized for imaging of living cells [81]. In this last configuration, the sample exposure is quite easy, not being required the sample encapsulation between two membranes, typically needed with other techniques, such as transmission electron microscopy (TEM) [82,83] or synchrotron-based microscopes [84]. Moreover, this configuration does not require the evacuation of the sample chamber, avoiding consequential problems related to eventual sample degassing due to incorrect sealing.

The setup allows irradiation of dried samples (in a vacuum) or wet samples (in a gaseous environment). For irradiation in a vacuum, the samples are mounted onto a rotational carousel, hosting up to 8 samples. For irradiation in a gaseous environment, the sample is mounted in a small cylindrical chamber filled with He, placed outside the source chamber. The two chambers are separated by a 200 nm thick Si_3N_4 membrane, ~16 mm from the plasma. A sample holder enables to load the PMMA-coated Si wafers, so that only a few mm gap between the sample and the separating membrane is filled with He gas at a pressure of ~1 bar. The He gas facilitates the removal of the air from the sample chamber, which, consequentially, efficiently attenuates the SXR radiation.

Sensitivity, contrast, and roughness depend on PMMA development conditions. The proper combination of those factors allows to achieve a high spatial resolution and, at the same time, the preservation of the biological structures investigated, avoiding affecting the region of the sample unexposed to SXR radiation [10].

A scheme of the SXR contact microscope is shown in Figure 12a. The employment of this technique does not require monochromatic radiation. Due to the employment of the Si_3N_4 filter, indeed, most of the required energy (2.8–4 nm) resides inside the "water window" spectral range (Figure 12b). Indeed, the K-edge of the filter blocks the lower energetic photons. Moreover, due to the limited energy of the laser pulse, and due to the limited gas-puff density, the generated plasma is not sufficiently hot to produce higher energy photons. The produced photon flux, measured by an AXUV 100 photodiode (Opto Diode Corporation, CA, USA), was ~8×10^8 photons/pulse at the PMMA surface, corresponding at an energy of 48.34 nJ. The experimental system is depicted in Figure 12c. More details can be found in references [85,86].
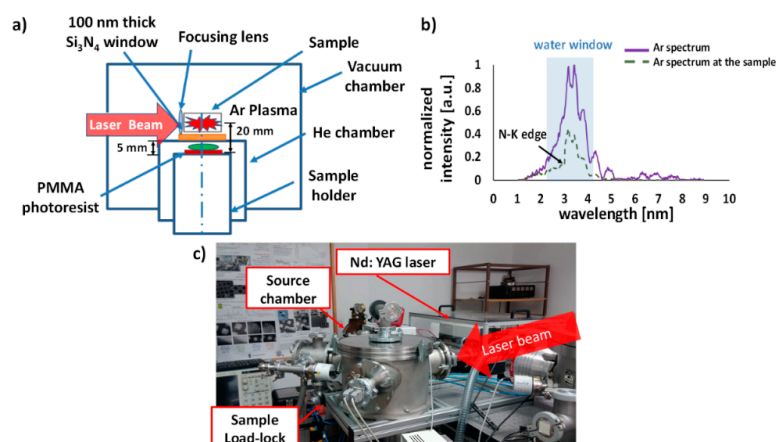

Figure 12. (**a**) Scheme of the SXR contact microscope setup. (**b**) Spectrum of Ar emission acquired directly from the plasma (continue, purple-line) and at the sample plane (dashed-green line). Image modified, based on [86]. (**c**) Picture of the SXR contact microscope system.

4. Biological Applications of EUV/SXR Microscopes Based on a Double Stream Gas-Puff Target Source

4.1. A 2D Full Field Imaging of Biological Samples

4.1.1. EUV Bioimaging

In this section, few biological samples, imaged with the EUV microscope, are commented on and discussed. All of the images were acquired at a 10 Hz source repetition rate, the detector temperature was −20 °C and the readout rate was $f_s = 50$ kHz. The presented images were acquired after 200 EUV pulses and a EUV exposure of ~20 s.

CT 26 Fibroblast Cells from Mus musculus Colon Carcinoma

The first image, presented in Figure 13, shows CT 26 fibroblast cells from *Mus musculus* mouse colon carcinoma (strain BALB/c). The samples were placed on top of a 30 nm Si_3N_4 membrane (from Silson Ltd., Warwickshire, England). The sample in Figure 13a was prepared with 30% hexamethyldisilazane (HDMS) in absolute ethanol (EtOH), while the sample in Figure 13b was prepared on top of a similar membrane, but with gradual dehydration in EtOH series (final concentration 70%), without any fixation procedure. The insets in Figure 13a,b, show small external features of the cells with a size varying from 60 to 120 nm. In the green line profile traced through the feature in the inset of Figure 13b (120 nm in size), the KE test (Figure 13c) was performed [71]. The slope, rising from 0 to 95%, indicates a Rayleigh (full-pitch) resolution of 66 nm, which corresponds to a 33 nm half-pitch spatial resolution. However, it should be taken into account that the feature that was imaged is not fully opaque and transmits some EUV radiation, so the conditions for the estimation of the KE resolution test were not totally fulfilled.
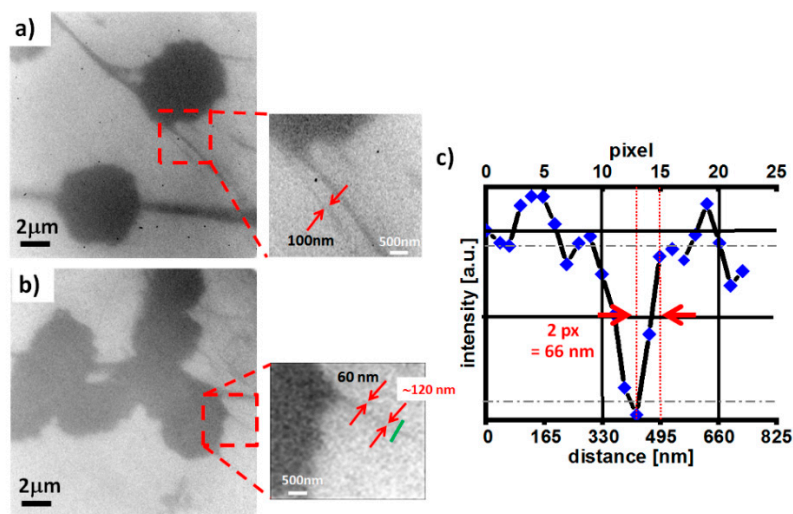

Figure 13. (**a**,**b**) EUV images of CT 26 fibroblast cells. Small features approaching the microscope resolution are shown in the zoomed insets. The zoom in (**b**) depicts the line profile through the smallest visible feature (indicated with a green line), showing a 0–95% slope rise of 66 nm. (**c**) Shows the KE test calculated over the green line of the (**b**) inset. Figure modified, based on [71,76].

Diatoms

Figure 14 shows a sample of diatoms, originally stored in a 60% EtOH solution, and later deposited on top of a 30 nm Si_3N_4 membrane. The sample was imaged with the optical microscope (a), and with the EUV microscope (b). EUV radiation allows resolving of external features, barely visible in the visible wavelength range, approaching the (half-pitch) spatial resolution of the microscope. However, as can be seen, the EUV radiation (b) is absorbed by the sample and it made the sample more opaque,

hiding the portion of the sample where the diatoms were mainly agglomerated. The insert shows a portion of the sample in which it was possible to resolve small features, of the order of ~135 nm.
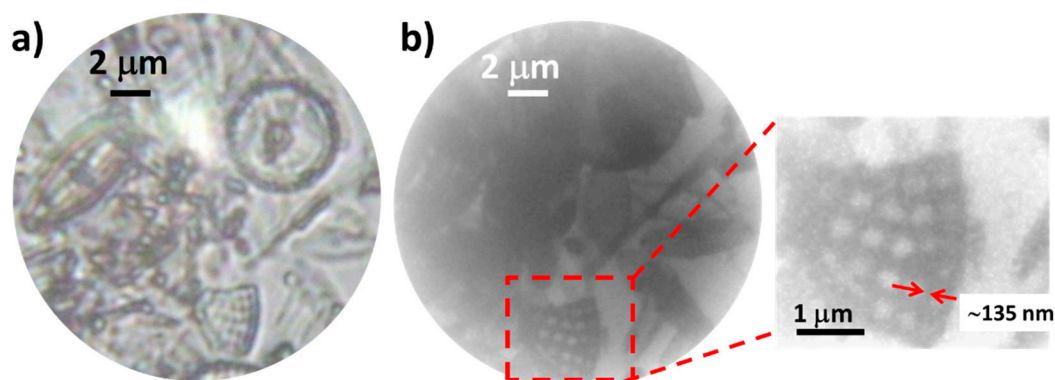

Figure 14. Images of diatoms acquired (**a**) with the optical microscope and (**b**) with the EUV microscope. The zoomed inset in (**b**) shows small features, of the order of 135 nm.

Chrysodidymus synuroideus Algae

A sample of dehydrated silica-scaled chrysophyte algae *Chrysodidymus synuroideus* was imaged. The cells, ~5 μm in size, having a skeleton of siliceous scales, consisting of a perforated base plate with a short apical spine.

The cells were cultured in DY-V Medium (Bigelow, ME, USA), at a growth temperature of 22 °C. The sample was fixed by a solution of 4% paraformaldehyde in phosphate-buffered saline (PBS) for 30 min at room temperature and then rinsed with PBS for 5 min. A series of EtOH-distilled water washes followed by air drying allowed the cells dehydration. A 10 μL drop of the suspension was deposited on the top of a 30 nm Si_3N_4 membrane. The imaged sample is presented in Figure 15a [87]. It was possible to resolve some dendrites thick from 100 to 50 nm approaching the microscope resolution, as shown in the detail of Figure 15b.
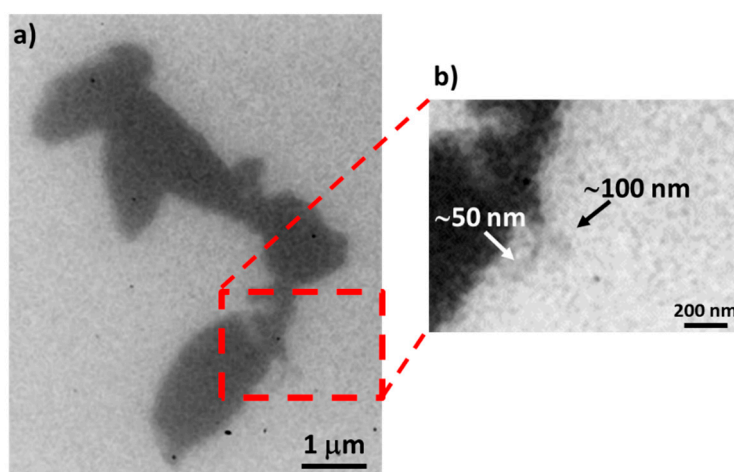
Figure 15. (**a**) *Chrysodidymus synuroideus* algae imaged with the EUV microscope. In (**b**) small features (~50–100 nm) are resolved. Figure modified, based on [76].

4.1.2. SXR Bioimaging

High contrast images, employing "water window" radiation were obtained due to a significant difference in absorption coefficients of biological sample constituents, i.e., water (oxygen) and carbon, enabling, in some cases, the observations of small features, approaching the half-pitch spatial resolution

of the microscope. Herein some biological samples imaged will be presented and discussed. For SXR image, an exposure from 1 to 600 SXR pulses was required, at a 10 Hz source repetition rate. The CCD camera was usually cooled down to −20 °C during the image acquisition, to decrease its intrinsic thermal noise and its readout was generally set to f_s = 2.5 MHz.

DNA Plasmids pBR322

A supercoiled, circular double stranded pBR322 plasmid DNA (from Inspiralis, Norwich, UK), was deposited on top of a 50 nm thick Si_3N_4 membrane, from a 100 ng/mL solution, subsequently dried in an N_2 atmosphere for 20 min [88]. The image shown in Figure 16a was acquired after 500 SXR pulses and an exposure time of 50 s. It is possible to observe DNA aggregations (from a few μm down to ~200 nm, as shown in Figure 16b [80]).
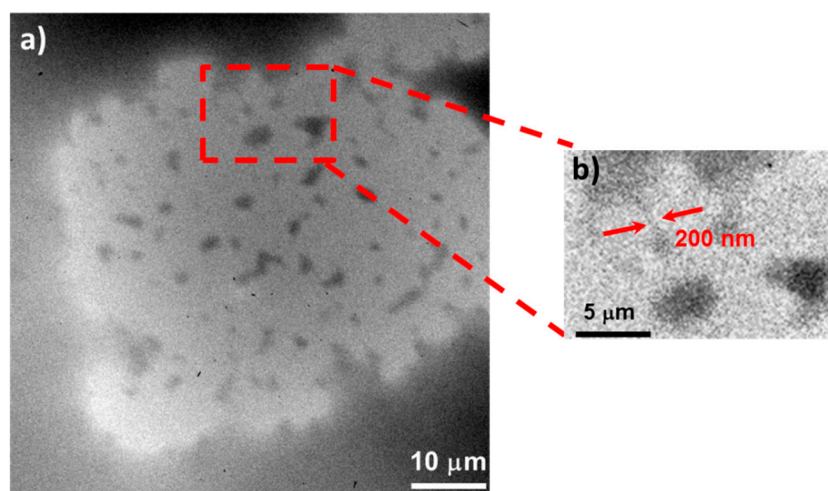
Figure 16. (**a**) Supercoiled pBR322 plasmid DNA, deposited on top of a 50 nm thick Si_3N_4 membrane, from 100 ng/μL solution. The zoomed inset in (**b**) shows a 200 nm DNA segment. The image was acquired after 500 SXR pulses (50 s exposure). Figure based on [80].

CT 26 Fibroblasts Cells from Mus Musculus Colon Carcinoma

CT 26 fibroblasts were imaged also in the "water window" spectral range. The cells were dehydrated by a series of ethanol–distilled water washes and then cultured in Dulbecco's modified Eagle's medium (DMEM, Sigma-Aldrich, MO, USA). More details about the sample preparation are reported in [77]. After dehydration by a series of ethanol–distilled water washes, the sample was deposited on top of a 100 nm Si_3N_4 membrane.

In Figure 17a,c it is possible to observe the cells, 20–30 mm in size, imaged using an optical microscope (40× objective and NA = 0.7). The SXR images (Figure 17b–e), acquired with 600 SXR pulses, 1 min exposure, and a 50 kHz CCD readout speed, show enhanced spatial resolution due to the shorter employed wavelength, allowing to clearly observe internal and external structures of the cells. Moreover, the possibility to image small features of the order of ~60 nm, as shown in Figure 17e, demonstrate that the SXR microscope clearly goes beyond the capabilities obtainable employing classical visible light microscopy. However, it can be noted that, due to the dehydration shrinkage, in Figure 17b,d, it is possible to observe some distortions in the cell structure, as well as some radiation damages [76,77].

The same cell culture was prepared with gradual dehydration in EtOH series (final concentration 70%), without any fixation procedure, and deposited on top of a 30 nm thick Si_3N_4 membrane. Moreover, in this case it was possible to distinguish the internal structures of the cells. Figure 18 shows a direct comparison between the image acquired with an optical microscope (a,c) and with the SXR

microscope (b,d). The SXR image, acquired with 200 SXR pulses and an exposure time of 20 s, shows small features, of the order of ~240 nm [76,89,90].
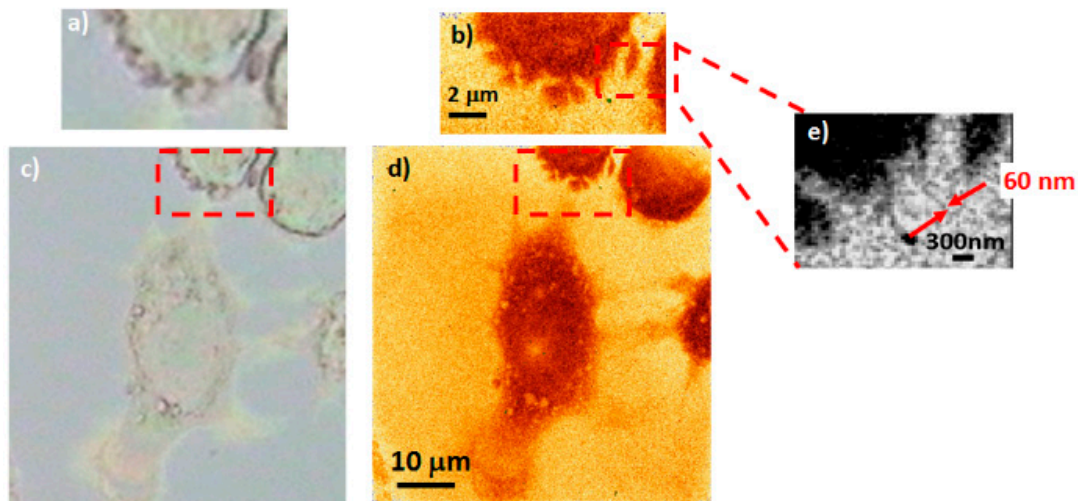

Figure 17. CT 26 fibroblasts from *Mus musculus* mouse colon carcinoma (strain BALB/c). Images acquired with visible light microscopy (**a**,**c**) and SXR ((**b**,**d**) presented in false colors). The internal structure is observable in (**a**,**c**) due to a phase-contrast and in (**b**,**d**) due to the modulation in the transmittance of the SXR radiation through the sample. The SXR images show enhanced spatial resolution and high absorption contrast. The zoomed image in (**e**) shows small features, approaching the half pitch spatial resolution of the SXR microscope (~60 nm). Acquisition parameters: 600 SXR pulses, 1 min. exposure. Figure modified, based on [77].
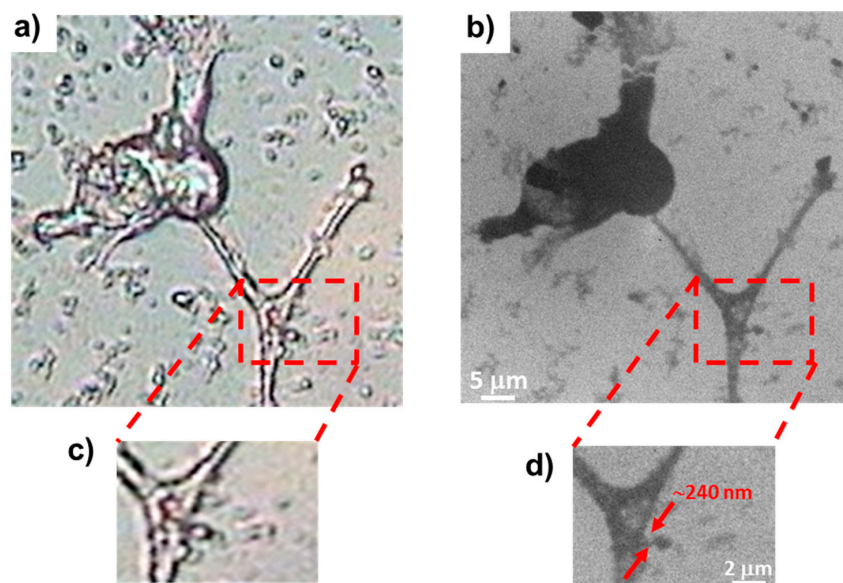
Figure 18. Sample of CT 26 fibroblast cells prepared with a final concentration of 70% EtOH. Comparison of (**a**) optical image and (**b**) SXR image. Insets (**c**,**d**) show small features imaged (indicated with red arrows in (**d**), of the order of 240 nm) that can be resolved only with the SXR microscope. The dehydration procedure by carbon-rich ethanol washes causes high SXR radiation absorption by the sample. Acquisition parameters: 200 SXR pulses, 20 s exposure. Figure based on [91].

Diatoms

A diatom sample preliminarily imaged with the optical microscope (Figure 19a), was then observed with the SXR "water window" microscope (Figure 19b) and with the EUV microscope

(Figure 19c). In this last case, it was possible to resolve some external features, barely visible in SXR range, approaching the (half-pitch) spatial resolution of the microscope. However, as can be seen, the EUV radiation is absorbed by the sample much more than the SXR radiation and allows to distinguish some internal features, as presented by the inset in Figure 19c [76].
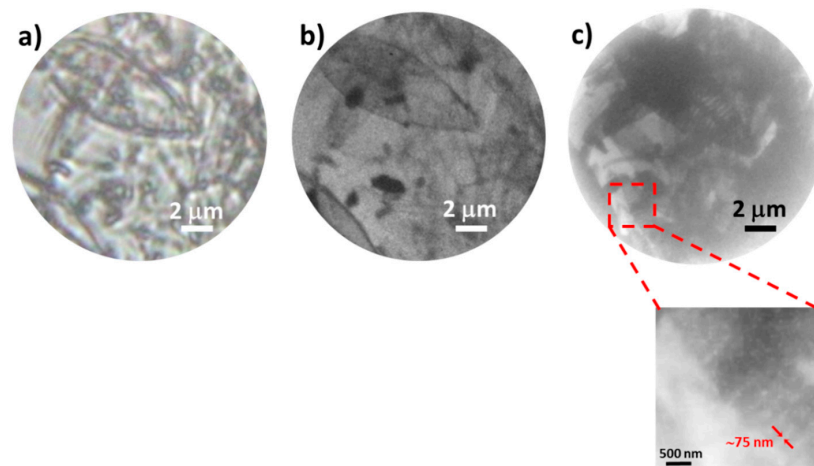

Figure 19. Direct comparison of diatoms, imaged with the visible (**a**), the SXR (**b**) and the EUV (**c**) microscope. In the zoomed picture of (**c**) are shown small features of ~75 nm. Acquisition parameters: 200 SXR pulses, 20 s exposure [91].

Chrysodidymus synuroideus Algae

A sample of dehydrated silica-scaled *Chrysodidymus synuroideus* algae was imaged. Figure 20 shows a comparison of the same sample imaged employing visible light (Figure 20a) and "water window" radiation (Figure 20b).
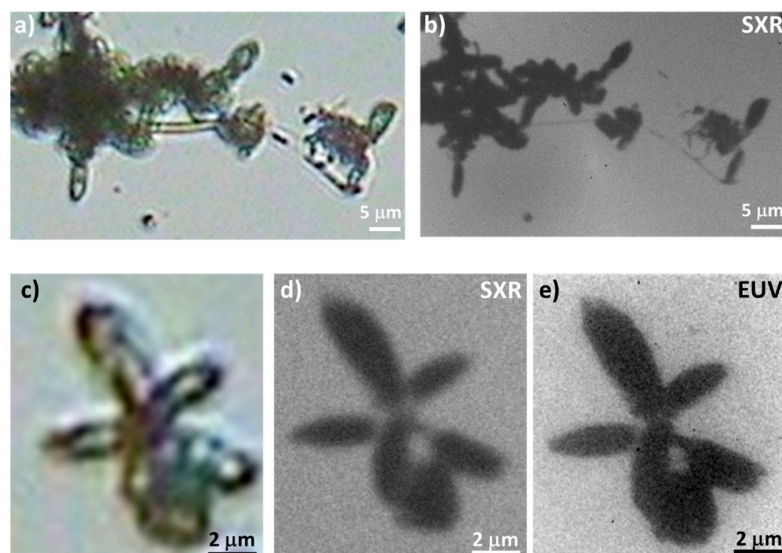
Figure 20. Direct comparison of *Chrysodidymus synuroideus* cells, imaged (**a**) with the optical microscope (visible light), (**b**) in the "water window" (acquired with 500 SXR pulses, 50 s exposure) and (**c**) in the EUV spectral range (acquired with 100 EUV pulses and 10 s exposure). (**c–e**) Show a direct comparison of a detail, imaged (**c**) with the visible light, (**d**) in the "water window" and (**e**) in the EUV spectral range [58].

In Figure 20b it is possible to observe that SXR gives a better image contrast, making possible to sharply resolve the external shape of some flagella, not visible in Figure 20a. An additional comparison

(Figure 20c,e) shows the same cell imaged employing visible light (Figure 20c), the "water window" radiation (Figure 20d), and the EUV radiation (Figure 20c). It is possible to see that the EUV image enhances the contrast of the image and so the external structure of the cell is clearly sharper and better visible than employing the SXR radiation. However, the fixing cell process, consisting of drying the sample using chemical substances rich in carbon (paraformaldehyde), made the cells opaque, hindering to observe internal [58].

Hippocampal Neurons from E17 Mouse Embryos

Figure 21a,b, shows a sample of hippocampal neurons from E17 mouse embryos. The neurons were cultured on poly-D-lysine coated in a 50 nm thick Si_3N_4 membrane and then fixed in 4% paraformaldehyde (PFA) in 20% sucrose PBS, followed by EtOH dehydration (from 100 to 70%) and final air-drying. The sample was first imaged using an optical microscope (Figure 21a, 40× objective, 400× magnification) and then with the SXR microscope (Figure 21b, in false colors), with an exposure of 200 SXR pulses (20 s) and a magnification of 410×. The high absorption coefficient in the "water window" spectral range enhances the optical contrast, showing a significant improvement of the spatial resolution. This is proven by the comparison of Figure 21, where a barely visible neuron in Figure 21a is much better resolved in Figure 21b, distinguishing, sharply, even some neuron dendrites [89].
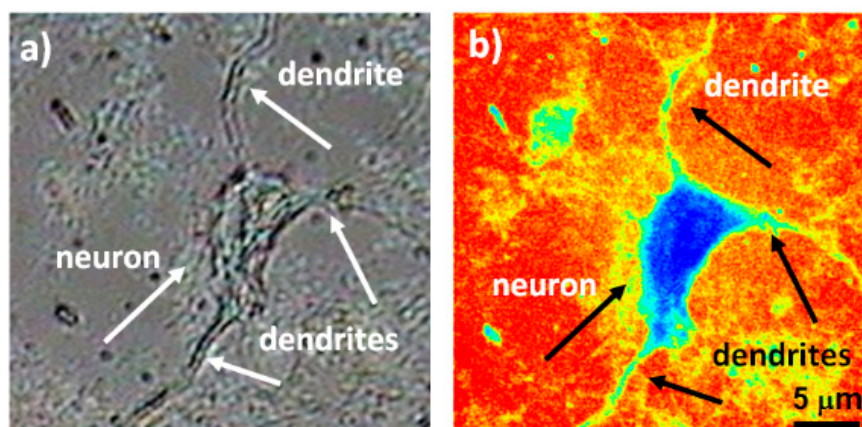

Figure 21. Comparison of the mouse hippocampal neuron acquired (**a**) with an optical microscope (40× objective, 400×) and (**b**) SXR microscope (in false colors), showing a single neuron with dendrites branching out. Image acquired after 200 SXR pulses, 20 s exposure. Figure (**a**) from [76].

4.2. Angular Projection SXR Tomography for Biological Nanoimaging

Few samples were imaged to test and demonstrate the possibility to perform tomographic experiments. Herein we will present the main results achieved up to now, which will be further improved.

4.2.1. Hep-2 Cells Crystals

A sample of liver cancer cells HEp-2 cells (human larynx epidermoid carcinoma cell line) was imaged. The cells were fixed in 4% paraformaldehyde in 0.5 mL of PBS medium. A 3 μL drop of solution was deposited on top of a 30 nm Si_3N_4 membrane and dried in an N_2 atmosphere. In this case, due to the low density of cells in the sample drop, it was possible to observe only the crystals formed from the PBS medium, as shown in Figure 22a, which was acquired with an optical microscope (40× objective). The image chosen for SXR tomography, marked with a red rectangle (Figure 22b), was obtained at a magnification of 100× with a FOV of $100 \times 60 \ \mu m^2$. Some acquired projections (in an angular range of 0°–54°) are shown in Figure 22c. The images were acquired using the internal camera. The presented images were obtained cropping the full-frame CCD image to FOV of $100 \times 60 \ \mu m^2$. It is possible to observe that starting from 42° the FOV results darker, because the edge of the membrane supporting the sample becomes visible (from the right side to the left) and, in other words, thicker,

increasing the SXR light path length in the membrane. From the 12° projection, it is observable damage (crack) of the membrane, which becomes more visible at larger angles, where part of the membrane goes behind the intact part and the darker region (i.e. where the SXR radiation propagates), which is perpendicularly deformed from the image plane and is visible only for larger angle projections [59,92].
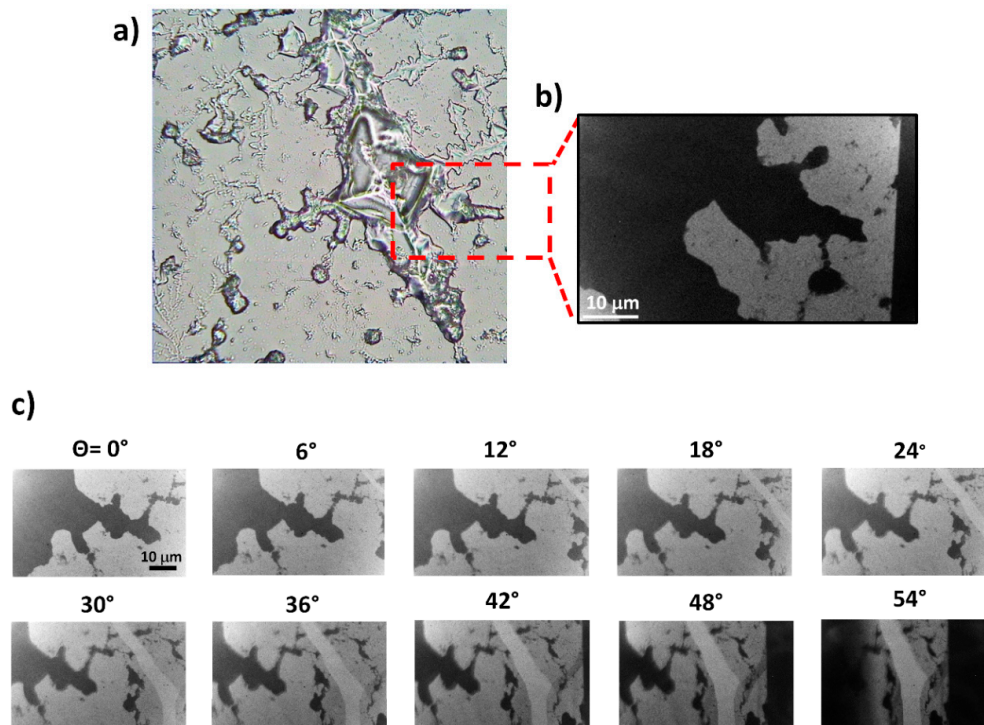

Figure 22. HEp-2 cells (human larynx epidermoid carcinoma cell line) in phosphate-buffered saline (PBS) medium on top of a 30 nm thick membrane. (**a**) Shows an optical microscope picture (visible light) acquired with a 40× objective. (**b**) Shows the region of the membrane imaged in SXR, which was then acquired at different angles with the SXR tomographic system. (**c**) From the 12° projection, it is possible to observe the broken and out of plane Si_3N_4 membrane. Figure modified, based on [59].

4.2.2. Caffeine Fibers

An interesting imaged sample was a caffeine crystal (caffeine anhydrous from the International Trade Center, ITC, purity 98.9–100%) dissolved in an aqueous solution. During the drying process, elongated caffeine crystals were created and subsequently deposited on top of the tip-holder, as shown in the SEM image of Figure 23a. Keeping our attention to a small fiber, enhanced with the rectangular detail in Figure 23a, it was possible to image the sample in the full angle of rotation, from 0° to 360°, in steps of 10°. Some of the projections are shown in Figure 23b. It can be noted that the SEM image shows much more caffeine fibers than the SXR image because some fibers were detached from the tip during the venting-phase of the SEM and the subsequent transportation of the sample to the SXR tomography system. The imaged sample was then reconstructed using the ImageJ software [93,94]. A 3D reconstruction of the fiber surface (electron density) is shown in Figure 23c [59,92]. Although the shape of the sample was overall reconstructed, some features were not properly reproduced, because of the not homogeneous thicknesses of the fibers. A more accurate reconstruction was performed applying the generalized total iterative constraint strategy [95] under Rytov approximation (more details are reported in [96]). The support constraint in the spatial domain was calculated before the reconstruction, minimizing the generation of artifacts due to the limited angular range of the acquired projections [97] (Figure 23d). The estimated spatial resolution of the 3D reconstruction was ~1–2 μm for the single voxel size of $320 \times 320 \times 320$ nm^3.
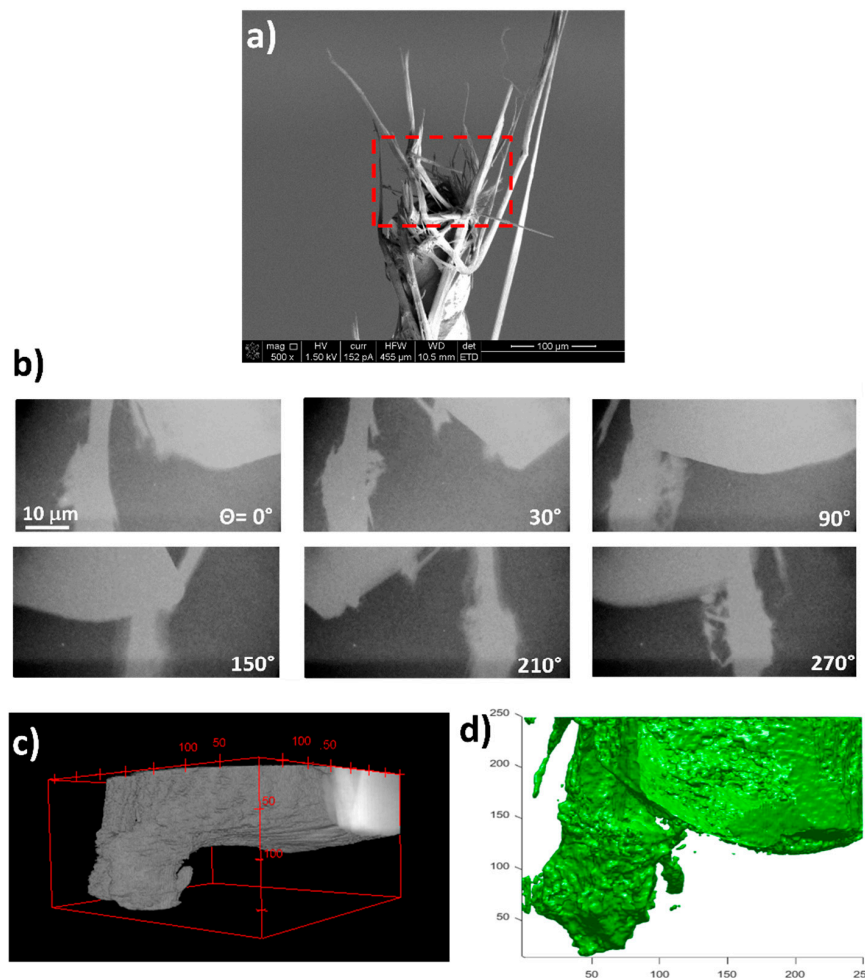
Figure 23. (**a**) SEM image of the caffeine crystals, on the top of the tip-sample holder. (**b**) Shows some of the projections acquired in SXR, at different angles. (**c**) Three-dimensional (3D) reconstruction of the reconstructed image of the crystallized caffeine (electron density surface) obtained using the ImageJ software [93,94]. (**d**) Crystals reconstruction using the total iterative constraint strategy. Figure modified, based on [59].

4.3. Imaging of Dried and Fixed Biological Samples Using Contact Microscopy

4.3.1. Non-Malignant Human Bladder HCV29 Cells

The developed contact microscope has been used for preliminary experiments acquiring SXR images by the AFM scanning of the surface of 500 nm thick PMMA photoresist of non-malignant human bladder HCV29 cell lines, particularly interesting for their elongated shape and well known morphological features. The cells were prepared following the protocol reported in [85,87]. The sample was then placed on top of a silicon wafer spin-coated PMMA. The imprint of cells on the PMMA photoresist was realized using a 1.5×1.5 mm^2, 100 nm thick Si_3N_4 window that filtered out the longer wavelengths above the SXR region. The produced relief-map of the cellular structures was then observed using an atomic force microscope (AFM, NT-MDT Spectrum Instruments, Moscow, Russia). In the SXR imprint HCV29 cells (Figure 24a–e) and their internal structures can be observed, at various scales of magnification. The AFM images of HCV29 cells with 150 nm diameter gold beads were obtained after 150 SXR pulses (15 s exposure, Figure 24a–c), and 20 SXR pulses (2 s exposure, Figure 24d,e) [85,87]. In the smallest scan of Figure 24e, 150 nm in diameter gold beads can also be seen. The KE test applied to those imprints suggests a spatial resolution of the order of 80 nm.
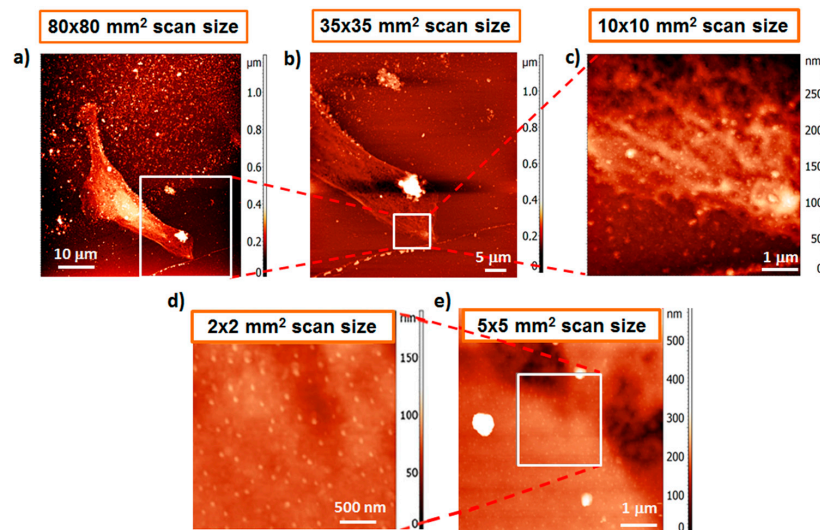
Figure 24. Soft X-ray contact microscopy images of HCV29 cells with 150 nm diameter gold beads obtained after 150 SXR pulses (15 s exposure, (**a**–**c**)) and 20 SXR pulses (2 s exposure, (**d**,**e**)) at different scan sizes. Figure modified, based on [85,87].

4.3.2. T24 Cancer Cells

A sample of T24 cells (transitional cancer cells of the urine bladder, ATCC®, Manassas, VA, USA) was imaged. The sample was prepared using a specific protocol, which enabled drying of the cells avoiding salt crystallization on its surface, according to the protocol reported in [76]. The images were acquired exposing the PMMA at 200 SXR pulses, for 20 s. After the cleaning procedure, performed using a 1% sodium hypochlorite solution, the photoresist was developed in methyl isobutyl ketone and isopropyl alcohol (MIBIK: IPA, 1:2 *v/v*) for 120 s, and finally observed by AFM, in a semi-contact mode, scanning an area of 80×80 μm^2 (corresponding to 512 pixels per line, Figure 25a) and of 25×25 μm^2 (1024 pixels per line, Figure 25b), respectively [76].
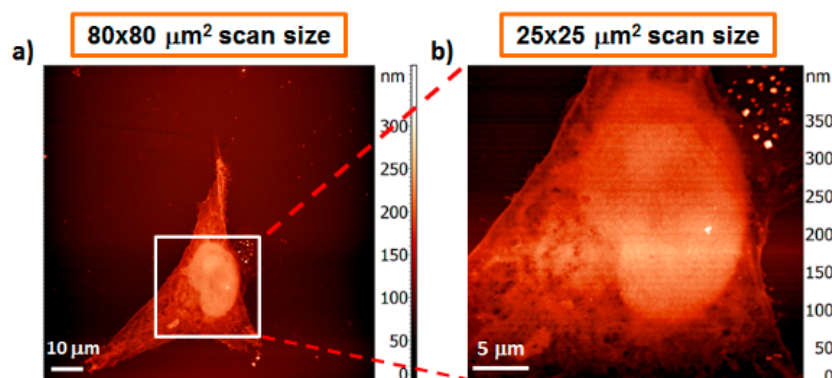
Figure 25. Soft X-ray images of fixed transitional cancer cell of the urine bladder (T24), field of view (FOV) = 80×80 μm^2 and 25×25 μm^2 (**a**,**b**). The images were acquired with exposure of 200 SXR pulses, 20 s exposure. Figure modified, based on [76].

4.3.3. Epidermal Cells (Keratinocyte)

Epidermal cells (Keratinocytes) were cultured on a PMMA photoresist. The employed culture medium DMEM (Sigma-Aldrich) was washed with a PBS buffer solution and then fixed and dehydrated using PFA 3.7% in PBS at 35 °C. The sample was imaged exposing the PMMA at 200 SXR pulses for 20 s The images, shown in Figure 26, were acquired by scanning the photoresist by AFM, over an

area of $60 \times 60 \ \mu m^2$ (a) and $25 \times 25 \ \mu m^2$ (b), 512 pixels per line. It was possible to achieve a half-pitch spatial resolution of ~80 nm, observing structures with sizes below 100 nm [67].
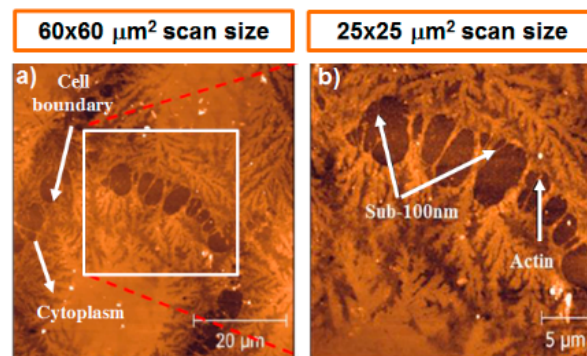

Figure 26. Soft X-ray images of fixed epidermal cells (Keratinocytes), FOV = $60 \times 60 \ \mu m^2$ (**a**) and $25 \times 25 \ \mu m^2$ (**b**). Structures with sizes below 100 nm are visible. The photoresist was scanned using an atomic force microscope (AFM) in semi-contact mode. The images were acquired with SXR exposure of 200 pulses, 20 s exposure. Figure modified, based on [67].

4.3.4. Imaging of Various Cell Lines

A further study was devoted to investigating the effect of the SXR radiation absorbed energy on the contact microscopy imprint preparation. The following human cell lines were imaged: prostate DU145 prostate carcinoma cells (AHTB-81, from ATCC®, VA, USA), HCC38 breast cancer cells (CRL-2314TM, from ATCC®, VA, USA), and human bone marrow-derived mesenchymal stem cells hMSC (Poietics™, PT-2501, from Lonza, MD, USA). Details about the sample preparation are reported in [86]. The optical microscope images (Figure 27a–c), acquired using a Primovert microscope (from Zeiss, Oberkochen, Germany) show the different morphology of the cell lines. In particular, the DU145 cell line (Figure 27a) present different shapes and sizes compared to HCC38 and hMSC cells (Figure 27b,c, respectively). HCC38 and hMSC cell lines are, indeed, much bigger and elongated. hMSCs cells, extending up to 400 μm in length, have a thickness of 2.5–3.5 μm. DU145 prostate carcinoma cells, instead, having a rhombic shape, are smaller and thicker (~6 μm).
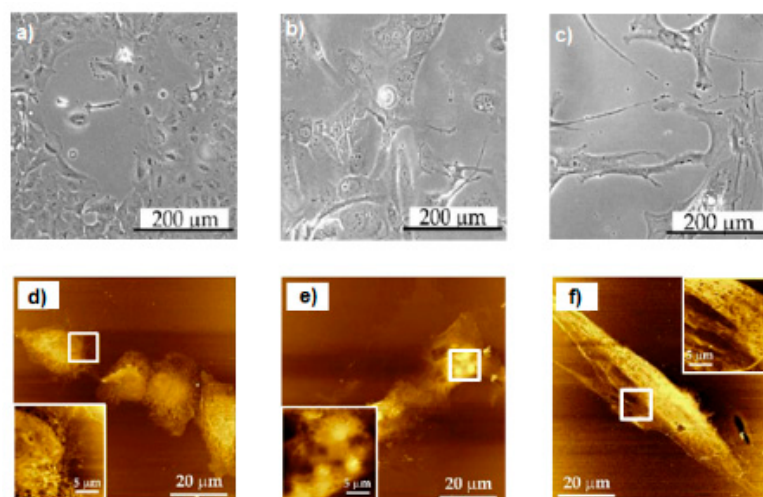

Figure 27. Images acquired using an inverse optical microscope with a 20x objective of (**a**) DU145 prostate cancer cells, (**b**) HCC38 breast cancer cells, (**c**) hMSC (human mesenchymal stem cells). On the bottom of each image are depicted the respective SXR contact microscopy images (**d**–**f**). The images were obtained with exposure of 800 SXR pulses. Results were collected using AFM (scan size: $80 \times 80 \ \mu m^2$). The insets ($80 \times 80 \ \mu m^2$) shows fragments of detailed cellular structures. Figure modified, based on [86].

The PMMA of the samples was exposed to 800 SXR and then developed with MIBK: IPA, in an optimal ratio of 1:2. AFM imaging, using a CP-II, Veeco, CA, USA, with MPP-11123-10 cantilevers, was performed in tapping mode. In the rhombical DU145 cells, smaller in size and agglomerate, was not possible to visualize internal structures (Figure 27d), while, instead, in the HCC38 cells, larger, it was possible to observe the cell nuclei, distinguishing also several nucleoli (Figure 27e). Finally, in the hMSCs cells, which are the largest imaged, even though the nucleus was barely visible, it was possible to clearly visualize the edges of the cell membrane and the internal cytoskeleton elements (Figure 27f).

5. Discussion and Conclusions

Progress in science requires the investigation of nanostructures on the micro- and nano-scales. Employing short wavelength radiation, it was possible to develop compact Fresnel zone plates based microscopes performing imaging experiments in transmission mode and overpassing the limited accessibility and high costs of large facilities such as synchrotrons and XFEL installations. Microscopes based on laser-plasma EUV and SXR sources with double stream gas-puff targets, coupled with diffractive optics, such as FZPs, represent a good way to perform experiments in small scales, achieving sub-100 nm half-pitch spatial resolution, and represent an important alternative for high-resolution imaging, which can be employed for different applications, opening the possibility of their widespread and commercialization in the near future.

The laser-plasma source based on a double stream gas-puff target was successfully optimized for efficient generation of radiation in the SXR range, developing a desktop "water window" microscope, based on emission at a wavelength of 2.88 nm from N_2 ions. Such a system, easily accessible and simple to use, allows acquiring magnified images of the objects with a 60 nm half-pitch spatial resolution, magnification (sample to CCD) of 220× or higher, and exposure time as low as a few seconds. Exploiting a natural, optical contrast in the "water window" spectral range, the microscope represents a very useful tool for biological, materials science, and nanotechnology imaging applications, and may be considered as a complementary imaging system to other already well-established techniques.

A compact stand-alone transmission microscope, employing an Ar-based double stream gas-puff target EUV source, under incoherent illumination, operating at a 13.84 nm wavelength, close to the lithography one (of 13.5 nm), with a sub-50 nm half-pitch spatial resolution. Such a system, developed as a demonstrator, can be employed for semiconductor applications as well as for nanotechnology, material science, and nano-lithographic mask inspections, to observe small features with high-resolution. Moreover, due to the high contrast, the EUV radiation enables the study of thin external cell features, such as the morphology of the cellular membranes, thanks to the absorption of the EUV light in carbon.

A contact-type microscopy system using a laser-produced plasma soft X-ray source operating in the "water window" spectral range was also developed. The applicability of the source for contact microscopy experiments was demonstrated by acquiring images of biological samples. From the presented results, a half-pitch spatial resolution of ~80 nm was successfully achieved. Although contact microscopy allows acquiring images with high spatial resolution without the need for expensive tools and optics, it is limited by the resolution of the photoresist, which can be destroyed during the SXR irradiation. Therefore it was demonstrated that the contact soft X-ray microscopy can efficiently provide complementary information concerning biological samples, integrating other existing microscopy techniques.

The photon fluxes obtained with the gas-puff source allow performing high-resolution imaging experiments. The flux achieved with EUV radiation, of 1.36×10^{11} photons/s for a single pulse, is comparable (or even higher) to that obtainable employing other compact systems. Laser-plasma EUV sources for lithography are currently capable to obtain a flux of 10^8 photons/s [98], while ptychography sources enable a gain of 10^{11} photons/s at 18 nm [99]. Recent progress pushed forward this limit, obtaining up to ~2×10^{12} photons/s with compact systems employing HHG [100].

Depending on the experiment performed in the SXR range, the gas-puff target source permits to achieve a photon flux in the range of 10^9–10^{11} photons/pulse. Such values fit with that obtained using

other compact systems operating in the "water window" spectral range such as capillary discharge [101] and X-ray absorption spectroscopy [102], allowing to obtain a photon flux of ~10^9 photons/s.

The presented microscopes offer a superior spatial resolution to the visible light (optical) microscopes and, in contrast to other microscopy techniques such as SEM or TEM, do not require a preliminary special preparation of the samples to image. Although the spatial resolution achieved cannot compete with the SEM, it has to be taken into account that the EUV/SXR microscopes still operate using photons (with higher energy), instead of electrons. Thus, the photons-matter interaction allows obtaining different information from the sample, which can be integrated with the SEM one, based on electron-matter interaction. Moreover, despite the resolution of the presented microscopes is similar to that achievable with the stimulated emission depletion microscope (STED) in the visible light region [103], they allow the acquisition of full field images, contrary to STED systems, which operates in scanning mode, without the requirement of any fluorescence markers or staining, which modify the sample to be imaged. The resolution of the compact microscopes can be improved by employing a zone plate with a larger number of zones or by using high-repetition-rate lasers, to increase the photon flux on the sample plane and decrease the exposure time. The employment of a sub-pixel super-resolution camera in SXR represents also a solution to improve the actual achievements [62]. Moreover, the possibility to equip the presented full field microscopes with a cryo-stage, could make possible to image in vivo biological samples.

In conclusion, the presented SXR and EUV compact microscopes, providing high optical contrast, can be employed as complementary imaging tools to already existing, well-established ones, providing additional information about the investigated samples. Such microscopes bring together remarkable factors, such as the desktop size, fast exposures, and nanometer spatial resolution, opening the possibility to establish partnerships in university and laboratories or companies, and multidisciplinary collaborations in a wide scientific environment.

References

1. Attwood, D.T. *Soft X-rays and Extreme Ultraviolet Radiation*; Cambridge University Press (CUP): Cambridge, UK, 1999.
2. Rumsby, P.T. Laser produced plasmas as intense X-ray sources for microscopy at the Central Laser Facility. *J. Microsc.* **1985**, *138*, 245–265. [CrossRef]
3. NBSP. International Organization for Standardization (ISO). ISO 14813–1:2015. 2015. Available online: https://www.iso.org/obp/ui/#iso:std:iso:14813:-1:ed-2:v1:en (accessed on 26 October 2020).
4. Kördel, M.; Dehlinger, A.; Seim, C.; Vogt, U.; Fogelqvist, E.; Sellberg, J.A.; Stiel, H.; Hertz, H.M. Laboratory water-window X-ray microscopy. *Optica* **2020**, *7*, 658. [CrossRef]
5. Hädrich, S.; Rothhardt, J.; Krebs, M.; Demmler, S.; Limpert, J.; Tünnermann, A. High photon flux and repetition rate table-top EUV sources based on ultrashort pulse fiber lasers. In Proceedings of the 2015 IEEE Photonics Conference (IPC), Reston, VA, USA, 4–8 October 2015; pp. 72–73.
6. Ojeda, J.; Arrell, C.A.; Grilj, J.; Frassetto, F.; Mewes, L.; Zhang, H.; Van Mourik, F.; Poletto, L.; Chergui, M. Harmonium: A pulse preserving source of monochromatic extreme ultraviolet (30–110 eV) radiation for ultrafast photoelectron spectroscopy of liquids. *Struct. Dyn.* **2016**, *3*, 023602. [CrossRef] [PubMed]
7. Spiller, E.; Segmüller, A.; Rife, J.; Haelbich, R. Controlled fabrication of multilayer soft-X-ray mirrors. *Appl. Phys. Lett.* **1980**, *37*, 1048–1050. [CrossRef]
8. Ortega, R.; Bohic, S.; Tucoulou, R.; Somogyi, A.; Devès, G. Microchemical element imaging of yeast and human cells using synchrotron X-ray microprobe with Kirkpatrick−Baez optics. *Anal. Chem.* **2004**, *76*, 309–314. [CrossRef] [PubMed]
9. Snigirev, A.; Kohn, V.G.; Snigireva, I.; Lengeler, B. A compound refractive lens for focusing high-energy X-rays. *Nat. Cell Biol.* **1996**, *384*, 49–51. [CrossRef]
10. Kang, H.C.; Yan, H.; Winarski, R.P.; Holt, M.V.; Maser, J.; Liu, C.; Conley, R.; Vogt, S.; Macrander, A.T.; Stephenson, G.B. Focusing of hard x-rays to 16 nanometers with a multilayer Laue lens. *Appl. Phys. Lett.* **2008**, *92*, 221114. [CrossRef]
11. Chao, W.; Fischer, P.; Tyliszczak, T.; Rekawa, S.; Anderson, E.; Naulleau, P. Real space soft X-ray imaging at 10 nm spatial resolution. *Opt. Express* **2012**, *20*, 9777–9783. [CrossRef] [PubMed]
12. Legall, H.; Blobel, G.; Stiel, H.; Sandner, W.; Seim, C.; Takman, P.; Martz, D.H.; Selin, M.; Vogt, U.; Hertz, H.M.; et al. Compact X-ray microscope for the water window based on a high brightness laser plasma source. *Opt. Express* **2012**, *20*, 18362–18369. [CrossRef] [PubMed]
13. Yase, S.; Nagaya, K.; Mizoguchi, Y.; Yao, M.; Fukuzawa, H.; Motomura, K.; Yamada, A.; Ma, R.; Ueda, K.; Saito, N.; et al. Crossover in the photoionization processes of neon clusters with increasing EUV free-electron-laser intensity. *Phys. Rev. A* **2013**, *88*, 043203. [CrossRef]
14. Kashiwagi, S.; Kato, R.; Oyama, T.G.; Sakaue, K.; Masuda, A.; Nomoto, T.; Gowa, T.; Washio, M.; Kuroda, R.; Urakawa, J. Development of compact coherent EUV source based on laser Compton scattering. *Radiat. Phys. Chem.* **2009**, *78*, 1112–1115. [CrossRef]
15. Rösner, B.; Koch, F.; Döring, F.; Guzenko, V.A.; Meyer, M.; Ornelas, J.L.; Späth, A.; Fink, R.H.; Stanescu, S.; Swaraj, S.; et al. 7 nm Spatial Resolution in Soft X-ray Microscopy. *Microsc. Microanal.* **2018**, *24*, 272–273. [CrossRef]
16. CXRO-Center for X-ray Optics Database. Available online: http://henke.lbl.gov/optical_constants/ (accessed on 24 October 2020).
17. Wachulak, P.; Bartnik, A.; Fiedorowicz, H.; Panek, D.; Bruza, P. Imaging of nanostructures with sub-100 nm spatial resolution using a desktop EUV microscope. *Appl. Phys. A* **2012**, *109*, 105–111. [CrossRef]
18. Wachulak, P.; Torrisi, A.; Bartnik, A.; Węgrzyński, Ł.; Fok, T.; Jarocki, R.; Kostecki, J.; Szczurek, M.; Fiedorowicz, H. Fresnel zone plate telescope for condenser alignment in water-window microscope. *J. Opt.* **2015**, *17*, 055606. [CrossRef]

19. Wachulak, P.; Węgrzyński, Ł.; Zápražný, Z.; Bartnik, A.; Fok, T.; Jarocki, R.; Kostecki, J.; Szczurek, M.; Korytár, D.; Fiedorowicz, H. Extreme ultraviolet tomography using a compact laser-plasma source for 3D reconstruction of low density objects. *Opt. Lett.* **2014**, *39*, 532–535. [CrossRef]

20. Park, I.Y.; Choi, J.; Lee, D.-H.; Han, S.; Kim, S.; Kim, S.-W. Generation of EUV radiation by plasmonic field enhancement using nano-structured bowties and funnel-waveguides. *Ann. Phys.* **2012**, *525*, 87–96. [CrossRef]

21. Li, L.; Liu, X.; Pal, S.; Wang, S.; Ober, C.K.; Giannelis, E.P. Extreme ultraviolet resist materials for sub-7 nm patterning. *Chem. Soc. Rev.* **2017**, *46*, 4855–4866. [CrossRef]

22. DiCicco, D.S.; Kim, D.; Rosser, R.; Suckewer, S. First stage in the development of a soft-x-ray reflection imaging microscope in the Schwarzschild configuration using a soft-X-ray laser at 182 nm. *Opt. Lett.* **1992**, *17*, 157–159. [CrossRef]

23. Vaschenko, G.; Brizuela, F.; Brewer, C.; Grisham, M.; Mancini, H.; Menoni, C.S.; Marconi, M.C.; Rocca, J.J.; Chao, W.; Liddle, J.A.; et al. Nanoimaging with a compact extreme-ultraviolet laser. *Opt. Lett.* **2005**, *30*, 2095–2097. [CrossRef]

24. Brewer, C.A.; Brizuela, F.; Wachulak, P.; Martz, D.H.; Chao, W.; Anderson, E.H.; Attwood, D.T.; Vinogradov, A.V.; Artyukov, I.A.; Ponomareko, A.G.; et al. Single-shot extreme ultraviolet laser imaging of nanostructures with wavelength resolution. *Opt. Lett.* **2008**, *33*, 518–520. [CrossRef]

25. Wachulak, P.; Marconi, M.C.; Bartels, R.A.; Menoni, C.S.; Rocca, J.J. Sub-50nm extreme ultraviolet holographic imaging. In *Proceedings of the Holography: Advances and Modern Trends*; SPIE-International Society of Optical Engineering: Bellingham, WA, USA, 2009; Volume 7358, p. 735806.

26. Kasuya, K.; Kolacek, K.; Schmidt, J.; Frolov, O.; Straus, J.; Matejicek, J.; Choukoulov, A.; Motokoshi, S.; Nakai, M.; Tokunaga, K. Surface changes of structural materials ablated with nanosecond EUV laser light. In Proceedings of the 16th Symposium on Advanced Photon Research, Kizugawa, Kyoto, Japan, 15–16 October 2015. [CrossRef]

27. Brewer, C.; Vaschenko, G.; Brizuela, F.; Wang, Y.; Larotonda, M.A.; Luther, B.M.; Marconi, M.C.; Rocca, J.J.; Menoni, C.S.; Chao, W.; et al. Sub-38 nm resolution microscopy with a tabletop 13 nm wavelength laser. In Proceedings of the 2006 Conference on Lasers and Electro-Optics and 2006 Quantum Electronics and Laser Science Conference, Long Beach, CA, USA, 21–26 May 2006; Volume 31, pp. 1–2. [CrossRef]

28. Mey, T.; Rein, M.; Großmann, P.; Mann, K. Brilliance improvement of laser-produced soft x-ray plasma by a barrel shock. *New J. Phys.* **2012**, *14*, 073045. [CrossRef]

29. Wieland, M.; Spielmann, C.; Kleineberg, U.; Westerwalbesloh, T.; Heinzmann, U.; Wilhein, T.; Spielmann, C. Toward time-resolved soft X-ray microscopy using pulsed fs-high-harmonic radiation. *Ultramicroscopy* **2005**, *102*, 93–100. [CrossRef] [PubMed]

30. Kishimoto, M.; Tanaka, M.; Tai, R.; Sukegawa, K.; Kado, M.; Hasegawa, N.; Tang, H.; Kawachi, T.; Lu, P.; Nagashima, K.; et al. Development of soft X-ray microscopy system using X-ray laser in JAERI Kansai. *J. Phys. IV Fr.* **2003**, *104*, 141–143. [CrossRef]

31. Zürch, M.; Jung, R.; Späth, C.; Tümmler, J.; Guggenmos, A.; Attwood, D.; Kleineberg, U.; Stiel, H.; Spielmann, C. Transverse coherence limited coherent diffraction imaging using a Molybdenum Soft X-ray Laser Pumped at Moderate Pump Energies. *Sci. Rep.* **2017**, *7*, 5314. [CrossRef]

32. Cardin, V.; Schimdt, B.E.; Thiré, N.; Beaulieu, S.; Wanie, V.; Negro, M.; Vozzi, C.; Tosa, V.; Légaré, F. Self-channelled high harmonic generation of water window soft X-rays. *J. Phys. B At. Mol. Opt. Phys.* **2018**, *51*, 174004. [CrossRef]

33. Frank, V.; Chushkin, Y.; Fröhlich, B.; Abuillan, W.; Rieger, H.; Becker, A.S.; Yamamoto, A.; Rossetti, F.F.; Kaufmann, S.; Lanzer, M.; et al. Lensless tomographic imaging of near surface structures of frozen hydrated malaria-infected human erythrocytes by coherent X-ray diffraction microscopy. *Sci. Rep.* **2017**, *7*, 14081. [CrossRef]

34. Treacher, D.J.; Lloyd, D.T.; Wiegandt, F.; O'Keeffe, K.; Hooker, S.M. Optimised XUV holography using spatially shaped high harmonic beams. *Opt. Express* **2019**, *27*, 29016–29025. [CrossRef]

35. Chen, Z.; Odstrcil, M.; Jiang, Y.; Han, Y.; Chiu, M.-H.; Li, L.-J.; Muller, D.A. Mixed-state electron ptychography enables sub-angstrom resolution imaging with picometer precision at low dose. *Nat. Commun.* **2020**, *11*, 2994. [CrossRef]

36. Helk, T.; Zürch, M.; Spielmann, C. Perspective: Towards single shot time-resolved microscopy using short wavelength table-top light sources. *Struct. Dyn.* **2019**, *6*, 010902. [CrossRef]

37. Wenz, J.; Schleede, S.; Khrennikov, K.; Bech, M.; Thibault, P.; Heigoldt, M.; Pfeiffer, F.; Karsch, S. Quantitative X-ray phase-contrast microtomography from a compact laser-driven betatron source. *Nat. Commun.* **2015**, *6*, 7568. [CrossRef]

38. Johansson, G.A.; Holmberg, A.; Hertz, H.M.; Berglund, M. Design and performance of a laser-plasma-based compact soft X-ray microscope. *Rev. Sci. Instrum.* **2002**, *73*, 1193–1197. [CrossRef]

39. Benk, M.; Bergmann, K.; Schäfer, D.; Wilhein, T. Compact soft X-ray microscope using a gas-discharge light source. *Opt. Lett.* **2008**, *33*, 2359–2361. [CrossRef] [PubMed]

40. Legall, H.; Stiel, H.; Blobel, G.; Seim, C.; Baumann, J.; Yulin, S.; Esser, D.; Hoefer, M.; Wiesemann, U.; Wirtz, M.; et al. A compact laboratory transmission X-ray microscope for the water window. In Proceedings of the Journal of Physics: Conference Series; IOP Publishing: Bristol, UK, 2013; Volume 463, pp. 5–10.

41. Martz, D.H.; Selin, M.; Von Hofsten, O.; Fogelqvist, E.; Holmberg, A.; Vogt, U.; LeGall, H.; Blobel, G.; Seim, C.; Stiel, H.; et al. High average brightness water window source for short-exposure cryomicroscopy. *Opt. Lett.* **2012**, *37*, 4425–4427. [CrossRef] [PubMed]

42. Müller, M.; Mey, T.; Niemeyer, J.; Mann, K. Table-top soft X-ray microscope using laser-induced plasma from a pulsed gas jet. *Opt. Express* **2014**, *22*, 23489–23495. [CrossRef]

43. Yu, Y.-S.; Farmand, M.; Kim, C.; Liu, Y.; Grey, C.P.; Strobridge, F.C.; Tyliszczak, T.; Celestre, R.; Denes, P.; Joseph, J.; et al. Three-dimensional localization of nanoscale battery reactions using soft X-ray tomography. *Nat. Commun.* **2018**, *9*, 921. [CrossRef]

44. Chiappi, M.; Conesa, J.J.; Pereiro, E.; Sorzano, C.O.S.; Rodríguez, M.J.; Henzler, K.; Schneider, G.; Chichón, F.J.; Carrascosa, J.L. Cryo-soft X-ray tomography as a quantitative three-dimensional tool to model nanoparticle:cell interaction. *J. Nanobiotechnology* **2016**, *14*, 15. [CrossRef]

45. Harkiolaki, M.; Darrow, M.C.; Spink, M.C.; Kosior, E.; Dent, K.; Duke, E. Cryo-soft X-ray tomography: Using soft X-rays to explore the ultrastructure of whole cells. *Emerg. Top. Life Sci.* **2018**, *2*, 81–92. [CrossRef]

46. Leontowich, A.F.; Berg, R.; Regier, C.N.; Taylor, D.M.; Wang, J.; Beauregard, D.; Geilhufe, J.; Swirsky, J.; Wu, J.; Karunakaran, C.; et al. Cryo scanning transmission X-ray microscope optimized for spectrotomography. *Rev. Sci. Instrum.* **2018**, *89*, 093704. [CrossRef]

47. Yabashi, M.; Tanaka, H. The next ten years of X-ray science. *Nat. Photon.* **2017**, *11*, 12–14. [CrossRef]

48. Kimura, T.; Joti, Y.; Shibuya, A.; Song, C.; Kim, S.; Tono, K.; Yabashi, M.; Tamakoshi, M.; Moriya, T.; Oshima, T.; et al. Imaging live cell in micro-liquid enclosure by X-ray laser diffraction. *Nat. Commun.* **2014**, *5*, 3052. [CrossRef]

49. Fiedorowicz, H.; Bartnik, A.; Jarocki, R.; Rakowski, R.; Szczurek, M. Enhanced X-ray emission in the 1-keV range from a laser-irradiated gas puff target produced using the double-nozzle setup. *Appl. Phys. A* **2000**, *70*, 305–308. [CrossRef]

50. Wachulak, P. Contributed Review: The novel gas puff targets for laser-matter interaction experiments. *Rev. Sci. Instrum.* **2016**, *87*, 091501. [CrossRef] [PubMed]

51. Wachulak, P.; Bartnik, A.; Jarocki, R.; Fiedorowicz, H. Characterization of multi-jet gas puff targets for high-order harmonic generation using EUV shadowgraphy. *Nucl. Instrum. Methods Phys. Res. Sect. B Beam Interact. Mater. Atoms* **2012**, *285*, 102–106. [CrossRef]

52. Rakowski, R.; Bartnik, A.; Fiedorowicz, H.; Jarocki, R.; Kostecki, J.; Mikolajczyk, J.; Szczurek, A.; Földes, I.; Tóth, Z.; Szczurek, M. Pulsed X-ray radiography of a gas jet target for laser–matter interaction experiments with the use of a CCD detector. *Nucl. Instrum. Methods Phys. Res. Sect. A Accel. Spectrom. Detect. Assoc. Equip.* **2005**, *551*, 139–144. [CrossRef]

53. Adjei, D.; Ayele, M.G.; Wachulak, P.; Bartnik, A.; Węgrzyński, Ł.; Fiedorowicz, H.; Vyšín, L.; Wiecheć, A.; Lekki, J.; Kwiatek, W.; et al. Development of a compact laser-produced plasma soft X-ray source for radiobiology experiments. *Nucl. Instrum. Methods Phys. Res. Sect. B Beam Interact. Mater. Atoms* **2015**, *364*, 27–32. [CrossRef]

54. Bartnik, A.; Fiedorowicz, H.; Wachulak, P. Spectral investigations of photoionized plasmas induced in atomic and molecular gases using nanosecond extreme ultraviolet (EUV) pulses. *Phys. Plasmas* **2014**, *21*, 073303. [CrossRef]

55. Rakowski, R.; Bartnik, A.; Fiedorowicz, H.; Jarocki, R.; Kostecki, J.; Krzywiński, J.; Mikołajczyk, J.; Pína, L.; Ryć, L.; Szczurek, M.; et al. Metrology of Mo/Si multilayer mirrors at 13.5 nm with the use of a laser-produced plasma extreme ultraviolet (EUV) source based on a gas puff target. *Opt. Appl.* **2006**, *36*, 593–600.

56. Wachulak, P.; Bartnik, A.; Jarocki, R.; Fok, T.; Węgrzyński, Ł.; Kostecki, J.; Szczurek, M.; Fiedorowicz, H. Study of uniformity of elongated plasma channels formed in gas puff targets using extreme ultraviolet and soft X-ray radiation. *Laser Part. Beams* **2015**, *33*, 293–298. [CrossRef]

57. Wachulak, P.; Bartnik, A.; Kostecki, J.; Węgrzyński, Ł.; Fok, T.; Jarocki, R.; Szczurek, M.; Fiedorowicz, H. Extreme ultraviolet and soft X-ray imaging with compact, table top laser plasma EUV and SXR sources. *Nucl. Instrum. Methods Phys. Res. Sect. B Beam Interact. Mater. Atoms* **2015**, *364*, 40–48. [CrossRef]

58. Torrisi, A.; Węgrzyński, Ł.; Fok, T.; Vondrová, Š.; Turňová, J.; Bartosewicz, B.; Wachulak, P.; Bartnik, A.; Parkman, T.; Jankiewicz, B.; et al. A stand-alone compact EUV microscope based on gas-puff target source. *J. Microsc.* **2016**, *265*, 251–260. [CrossRef]

59. Wachulak, P.W.; Torrisi, A.; Krauze, W.; Bartnik, A.; Kostecki, J.; Maisano, M.; Sciortino, A.M.; Fiedorowicz, H. A "water window" tomography based on a laser-plasma double-stream gas-puff target soft X-ray source. *Appl. Phys. A* **2019**, *125*, 70. [CrossRef]

60. Wachulak, P.W.; Torrisi, A.L.; Nawaz, M.F.; Adjei, D.; Bartnik, A.; Kostecki, J.; Wegrzynski, Ł.; Vondrová, Š.; Turňová, J.; Fok, T.; et al. A compact "water-window" microscope with 60-nm spatial resolution based on a double stream gas-puff target and Fresnel zone plate optics. In *Proceedings of the EUV and X-ray Optics: Synergy between Laboratory and Space*; SPIE-International Society for Optical Engineering: Bellingham, WA, USA, 2015; p. 95100M.

61. Werner, S.; Rehbein, S.; Guttmann, P.; Schneider, G. Three-dimensional structured on-chip stacked zone plates for nanoscale X-ray imaging with high efficiency. *Nano Res.* **2014**, *7*, 528–535. [CrossRef]

62. Lübcke, A.; Braenzel, J.; Dehlinger, A.; Schnürer, M.; Stiel, H.; Guttmann, P.; Rehbein, S.; Schneider, G.; Werner, S.; Kemmler, R.; et al. Soft X-ray nanoscale imaging using a sub-pixel resolution charge coupled device (CCD) camera. *Rev. Sci. Instrum.* **2019**, *90*, 043111. [CrossRef] [PubMed]

63. Kado, M.; Daido, H.; Yamamoto, Y.; Shinohara, K.; Richardson, M.C. Development of a laser plasma X-ray microscope to observe live hydrated biological specimens. *Laser Phys. Lett.* **2006**, *3*, 205–207. [CrossRef]

64. Sakdinawat, A.; Attwood, D.T. Nanoscale X-ray imaging. *Nat. Photon.* **2010**, *4*, 840–848. [CrossRef]

65. Kado, M.; Kishimoto, M.; Tamotsu, S.; Yasuda, K.; Shinohara, K. In situ observation of cellular organelles with a contact x-ray microscope. In *Proceedings of the Journal of Physics: Conference Series*; IOP Publishing: Bristol, UK, 2013; Volume 463, p. 012056.

66. Majima, T. Soft X-ray imaging of living cells in water: Flash contact soft X-ray microscope. *TrAC Trends Anal. Chem.* **2004**, *23*, 520–526. [CrossRef]

67. Ayele, M.; Wachulak, P.; Czwartos, J.; Adjei, D.; Bartnik, A.; Węgrzyński, Ł.; Szczurek, M.; Pina, L.; Fiedorowicz, H. Development and characterization of a laser-plasma soft X-ray source for contact microscopy. *Nucl. Instrum. Methods Phys. Res. Sect. B Beam Interact. Mater. Atoms* **2017**, *411*, 35–43. [CrossRef]

68. Fiedorowicz, H.; Bartnik, A. X-ray laser emission from a laser-irradiated gas puff target. *Bull. Pol. Acad. Sci. Tech. Sci.* **2005**, *53*, 103–111. [CrossRef]

69. Torrisi, A. Soft X-ray and Extreme Ultraviolet Nanoscale Imaging Using Compact Laser-Plasma Sources based on a Double Stream Gas-Puff Target and Fresnel Optics. Ph.D. Thesis, Military University of Technology, Warsaw, Poland, 10 April 2017.

70. Wachulak, P.; Bartnik, A.; Fiedorowicz, H.; Rudawski, P.; Jarocki, R.; Kostecki, J.; Szczurek, M. "Water window" compact, table-top laser plasma soft X-ray sources based on a gas puff target. *Nucl. Instrum. Methods Phys. Res. Sect. B Beam Interact. Mater. Atoms* **2010**, *268*, 1692–1700. [CrossRef]

71. Wachulak, P.; Torrisi, A.; Bartnik, A.; Węgrzyński, Ł.; Fok, T.; Fiedorowicz, H. A desktop extreme ultraviolet microscope based on a compact laser-plasma light source. *Appl. Phys. A* **2016**, *123*, 25. [CrossRef]

72. Marconi, M.C.; Wachulak, P. Extreme ultraviolet lithography with table top lasers. *Prog. Quantum Electron.* **2010**, *34*, 173–190. [CrossRef]

73. Kelly, R.L. Atomic and ionic spectrum lines below 2000 Angstroms: Hydrogen through Krypton Part I (H-Cr). *J. Phys. Chem. Ref. Data* **1987**, *16*, 1–404.

74. Heck, J.M.; Attwood, D.T.; Meyer-Ilse, W.; Anderson, E.H. Resolution determination in X-ray microscopy: An analysis of the effects of partial coherence and illumination spectrum. *J. X-Ray Sci. Technol.* **1998**, *8*, 95–104.

75. Torrisi, A.; Wachulak, P.; Bartnik, A.; Węgrzyński, Ł.; Fok, T.; Fiedorowicz, H. Development and optimization of a "water window" microscope based on a gas-puff target laser-produced plasma source. *EPJ Web Conf.* **2018**, *167*, 3002. [CrossRef]

76. Wachulak, P.; Torrisi, A.; Ayele, M.; Czwartos, J.; Bartnik, A.; Węgrzyński, Ł.; Fok, T.; Parkman, T.; Salačová, Š.; Turňová, J.; et al. Bioimaging using full field and contact EUV and SXR microscopes with nanometer spatial resolution. *Appl. Sci.* **2017**, *7*, 548. [CrossRef]

77. Wachulak, P.; Torrisi, A.; Nawaz, M.F.; Bartnik, A.; Adjei, D.; Vondrová, Š.; Turňová, J.; Jančarek, A.; Limpouch, J.; Vrbová, M.; et al. A compact "Water Window" microscope with 60 nm spatial resolution for applications in biology and nanotechnology. *Microsc. Microanal.* **2015**, *21*, 1214–1223. [CrossRef]

78. Engström, A. Microradiography and roentgen microscopy. In *Encyclopedia of Medical Radiology*; Springer Science and Business Media LLC: Berlin, Germany, 1967; Volume 3, pp. 677–693.

79. Torrisi, A.; Wachulak, P.; Nawaz, M.F.; Bartnik, A.; Węgrzyński, L.; Jancarek, A.; Fiedorowicz, H. Characterization and optimization of images acquired by a compact soft X-ray microscope based on a double stream gas-puff target source. *J. Instrum.* **2016**, *11*, C04003. [CrossRef]

80. Wachulak, P.; Torrisi, A.; Bartnik, A.; Adjei, D.; Kostecki, J.; Wegrzynski, L.; Jarocki, R.; Szczurek, M.; Fiedorowicz, H. Desktop water window microscope using a double-stream gas puff target source. *Appl. Phys. A* **2015**, *118*, 573–578. [CrossRef]

81. Ayele, M.G. Soft X-ray Contact Microscopy Using a Laser-Plasma Light Source Based on a Gas Puff Target. Ph.D. Thesis, Military University of Technology, Warsaw, Poland, 17 April 2018.

82. Sousa, A.A.; Leapman, R.D. Development and application of STEM for the biological sciences. *Ultramicroscopy* **2012**, *123*, 38–49. [CrossRef]

83. Pu, S.; Gong, C.; Robertson, A.W. Liquid cell transmission electron microscopy and its applications. *R. Soc. Open Sci.* **2020**, *7*, 191204. [CrossRef]

84. Jacobsen, C.; Kirz, J. X-ray microscopy with synchrotron radiation. *Nat. Genet.* **1998**, *5*, 650–653. [CrossRef] [PubMed]

85. Ayele, M.; Czwartos, J.; Adjei, D.; Wachulak, P.; Ahad, I.U.; Bartnik, A.; Węgrzyński, Ł.; Szczurek, M.; Jarocki, R.; Fiedorowicz, H.; et al. Contact microscopy using a compact laser produced plasma soft X-ray Source. *Acta Phys. Pol. A* **2016**, *129*, 237–240. [CrossRef]

86. Osuchowska, P.N.; Wachulak, P.; Nowak-Stępniowska, A.; Bartnik, A.; Gnanachandran, K.; Lekka, M.; Czwartos, J.; Fiedorowicz, H.; Trafny, E.A. Imaging of cell structures using optimized soft X-ray contact microscopy. *Appl. Sci.* **2020**, *10*, 6895. [CrossRef]

87. Wachulak, P.; Torrisi, A.; Ayele, M.; Czwartos, J.; Bartnik, A.; Jarocki, R.; Kostecki, J.; Szczurek, M.; Wegrzyński, Ł.; Fiedorowicz, H. Nanoscale imaging using a compact laser plasma source of soft X-rays and Extreme Ultraviolet (EUV). In *Springer Proceedings in Physics*; Springer Science and Business Media LLC: Berlin, Germany, 2018; Volume 202, pp. 251–260.

88. Adjei, D.; Wiecheć, A.; Wachulak, P.; Ayele, M.G.; Lekki, J.; Kwiatek, W.; Bartnik, A.; Davidkova, M.; Vyšín, L.; Juha, L.; et al. DNA strand breaks induced by soft X-ray pulses from a compact laser plasma source. *Radiat. Phys. Chem.* **2016**, *120*, 17–25. [CrossRef]

89. Wachulak, P.; Torrisi, A.; Ayele, M.; Bartnik, A.; Węgrzyński, Ł.; Fok, T.; Czwartos, J.; Fiedorowicz, H. Nanoimaging using soft X-ray and EUV sources based on double stream gas puff targets. *Acta Phys. Pol. A* **2018**, *133*, 271–276. [CrossRef]

90. Wachulak, P.; Torrisi, A.; Ayele, M.; Bartnik, A.; Czwartos, J.; Węgrzyński, Ł.; Fok, T.; Fiedorowicz, H. Nanoimaging using soft X-ray and EUV laser-plasma sources. *EPJ Web Conf.* **2018**, *167*, 3001. [CrossRef]

91. Torrisi, A.; Wachulak, P.W.; Bartnik, A.; Węgrzyński, Ł.; Fok, T.; Fiedorowicz, H. Biological and material science applications of EUV and SXR nanoscale imaging systems based on double stream gas puff target laser plasma sources. *Nucl. Instrum. Methods Phys. Res. Sect. B Beam Interact. Mater. Atoms* **2017**, *411*, 29–34. [CrossRef]

92. Wachulak, P.; Torrisi, A.; Krauze, W.; Bartnik, A.; Kostecki, J.; Maisano, M.; Fiedorowicz, H. Tomographic imaging using a compact soft X-ray microscope based on a laser plasma light source. In *EUV and X-ray Optics: Synergy between Laboratory and Space VI*; SPIE: Bellingham, WA, USA, 2019; Volume 11032, p. 110320N. [CrossRef]

93. *ImageJ*. Available online: http://imagej.nih.gov/ij/ (accessed on 20 May 2009).

94. MessaoudiI, C.; Boudier, T.; Sorzano, C.O.S.; Marco, S. TomoJ: Tomography software for three-dimensional reconstruction in transmission electron microscopy. *BMC Bioinform.* **2007**, *8*, 288. [CrossRef]

95. Krauze, W.; Makowski, P.; Kujawińska, M.; Kuś, A. Generalized total variation iterative constraint strategy in limited angle optical diffraction tomography. *Opt. Express* **2016**, *24*, 4924–4936. [CrossRef]

96. Devaney, A.J. Inverse-scattering theory within the Rytov approximation. *Opt. Lett.* **1981**, *6*, 374–376. [CrossRef]

97. Chambolle, A.; Pock, T. A first-order primal-dual algorithm for convex problems with applications to imaging. *J. Math. Imaging Vis.* **2011**, *40*, 120–145. [CrossRef]

98. Bleiner, D.; Staub, F.; Guzenko, V.; Ekinci, Y.; Balmer, J.E. Evaluation of lab-scale EUV microscopy using a table-top laser source. *Opt. Commun.* **2011**, *284*, 4577–4583. [CrossRef]

99. Eschen, W.; Tadesse, G.K.; Klas, R.; Tschernajew, M.; Tuitje, F.; Spielmann, C.; Tünnermann, A.; Limpert, J.; Rothhardt, J. High resolution ptychographic coherent diffractive imaging using table-top XUV sources. In *Imaging and Applied Optics 2018 (3D, AO, AIO, COSI, DH, IS, LACSEA, LS&C, MATH, pcAOP)*; Optical Society of America: Washington, DC, USA, 2018; p. JM3E.4. [CrossRef]

100. Keunecke, M.; Möller, C.; Schmitt, D.; Nolte, H.; Jansen, G.S.M.; Reutzel, M.; Gutberlet, M.; Halasi, G.; Steil, D.; Steil, S.; et al. Time-resolved momentum microscopy with a 1 MHz high-harmonic extreme ultraviolet beamline. *Rev. Sci. Instrum.* **2020**, *91*, 063905. [CrossRef] [PubMed]

101. Nawaz, M.; Nevrkla, M.; Jancarek, A.; Torrisi, A.; Parkman, T.; Turnova, J.; Stolcova, L.; Vrbova, M.; Limpouch, J.; Pina, L.; et al. Table-top water-window soft X-ray microscope using a Z-pinching capillary discharge source. *J. Instrum.* **2016**, *11*, P07002. [CrossRef]

102. Popmintchev, D.; Galloway, B.R.; Chen, M.-C.; Dollar, F.; Mancuso, C.A.; Hankla, A.; Miaja-Avila, L.; O'Neil, G.; Shaw, J.M.; Fan, G.; et al. Near- and extended-edge X-ray-absorption fine-structure spectroscopy using ultrafast coherent high-order harmonic supercontinua. *Phys. Rev. Lett.* **2018**, *120*, 093002. [CrossRef] [PubMed]

103. Hanne, J.; Falk, H.J.; Görlitz, F.; Hoyer, P.; Engelhardt, J.; Sahl, S.J.; Hell, S.W. STED nanoscopy with fluorescent quantum dots. *Nat. Commun.* **2015**, *6*, 7127. [CrossRef]

Publisher's Note: MDPI stays neutral with regard to jurisdictional claims in published maps and institutional affiliations.